doi.org/10.26434/chemrxiv.8870693.v1

Reducing the Pore Size of Covalent Organic Frameworks in Thin-Film Composite Membranes Enhances Solute Rejection

Amanda Corcos, Gabrielle Levato, Zhiwei Jiang, Austin Evans, Andrew Livingston, Benito Marinas, William Dichtel

Submitted date: 15/07/2019 • Posted date: 16/07/2019

Citation information: Corcos, Amanda; Levato, Gabrielle; Jiang, Zhiwei; Evans, Austin; Livingston, Andrew; Marinas, Benito; et al. (2019): Reducing the Pore Size of Covalent Organic Frameworks in Thin-Film Composite Membranes Enhances Solute Rejection. ChemRxiv. Preprint.

Three imine-linked covalent organic framework (COF) films are incorporated as active layers into separate thin-film composite (TFC) membranes and tested for their ability to reject an organic pollutant surrogate and salt from water. The synthesized membranes consist of a polyacrylonitrile (PAN) membrane supporting a TAPB-PDA-H, TAPB-PDA-Me, or TAPB-PDA-Et COF thin film. The latter two COFs direct six methyl and ethyl substituents per tiled hexagon into the pores, respectively, while maintaining the same topology across the series. These substituents decrease the effective pore size of the COF compared to the parent TAPB-PDA-H COF. The TAPB-PDA-Me membrane rejects Rhodamine-WT (R-WT) dye and NaCl better than the TAPB-PDA-H membrane, and the TAPB-PDA-Et membrane exhibits the best rejection overall. The solution-diffusion model used to analyze this permeation behavior indicates that there is a systematic difference in rejection as subsequent pendant groups are added to the interior of the COF pore. These findings demonstrate the concept of tuning the selectivity of COF membranes by systematically reducing the effective pore size within a given topology.

File list (3)

Reducing the Pore Size of Covalent Organic Frameworks in Thin-Film Composite Membranes Enhances Solute Rejection

Amanda R. Corcos,[1,‡] Gabrielle A. Levato,[2,‡] Zhiwei Jiang,[3] Austin M. Evans,[1] Andrew G. Livingston,[3] Benito J. Mariñas,[2] and William R. Dichtel[1,*]

[1]*Department of Chemistry, Northwestern University, 2145 Sheridan Road, Evanston, Illinois 60208, United States*

[2]*Safe Global Water Institute, Department of Civil and Environmental Engineering, University of Illinois at Urbana-Champaign, Urbana, Illinois 61801, United States*

[3]*Barrer Centre, Department of Chemical Engineering, Imperial College London, South Kensington Campus, Exhibition Road, London SW7 2AZ, United Kingdom*

ABSTRACT: Three imine-linked covalent organic framework (COF) films are incorporated as active layers into separate thin-film composite (TFC) membranes and tested for their ability to reject an organic pollutant surrogate and salt from water. The synthesized membranes consist of a polyacrylonitrile (PAN) membrane supporting a **TAPB-PDA-H**, **TAPB-PDA-Me**, or **TAPB-PDA-Et** COF thin film. The latter two COFs direct six methyl and ethyl substituents per tiled hexagon into the pores, respectively, while maintaining the same topology across the series. These substituents decrease the effective pore size of the COF compared to the parent **TAPB-PDA-H** COF. The **TAPB-PDA-Me** membrane rejects Rhodamine-WT (R-WT) dye and NaCl better than the **TAPB-PDA-H** membrane, and the **TAPB-PDA-Et** membrane exhibits the best rejection overall. The solution-diffusion model used to analyze this permeation behavior indicates that there is a systematic difference in rejection as subsequent pendant groups are added to the interior of the COF pore. These findings demonstrate the concept of tuning the selectivity of COF membranes by systematically reducing the effective pore size within a given topology.

Potable water is an increasingly limited resource because of the compounding effects of population growth, industrial pollution and economic development, and in many regions, the effects of climate change.[1] Inadequate sanitation and the re-use of inadequately treated wastewater represent additional sources of contamination. State-of-the-art pressure-driven membrane purification and desalination systems involve forcing contaminated and brackish water through nanofiltration (NF) and/or reverse osmosis (RO) thin-film composition (TFC) membranes with a thin (10-250 nm) active layer commonly made of fully- or semi-aromatic polyamide linkages.[2] These NF and RO systems are more energy efficient than evaporation methods, including multiple effect evaporation, yet still consume energy above the thermodynamic limit.[2] Polyamide membranes have been mostly developed and optimized empirically, which complicates tuning their separation behavior to specific separation challenges or water matrices. Because their pores cannot be controlled in a designed or atomically precise way, it is difficult to rationally improve their performance since there is a trade-off between energy consumption, flux, salt or pollutant rejection, and other performance characteristics.

Recently, 2D covalent organic frameworks (2D COFs) have emerged as a class of materials with precisely designed porosity, topology, and chemical functionality.[3-10] These attributes make COFs promising candidates for molecularly engineered membranes since, by careful selection of the monomer subunits which are then polymerized into layered sheets, membranes can be engineered at the molecular level. To date, hundreds of structurally and chemically unique COFs have been synthesized. However, most COFs have only been synthesized as microcrystalline powders, which bottlenecks their promise for use in membranes. The ability to control material morphology, whether into crystalline films,[11-12] monolithic blocks,[13] or colloidal suspensions,[14-16] represents a major frontier in 2D polymer science.

Scheme 1.

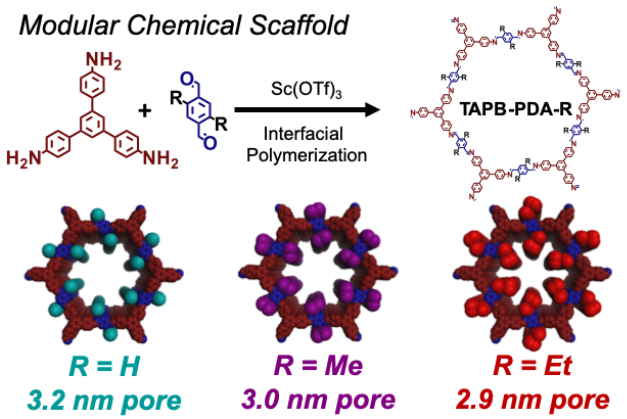

Capitalizing on the ability to form crystalline, free-standing COF films, early studies have focused on incorporating these films into membranes and examining their ability to separate trace contaminants from solution, many of which have been described in recent

reviews.[17-19] We have shown that the imine-linked **TAPB-PDA-H** COF forms as a film via interfacial polymerization at either the liquid/liquid or liquid/air interface when a $Sc(OTf)_3$ catalyst is phase segregated from the **TAPB** and **PDA** monomers.[20-21] The resulting films range in thickness from 100 μm down to 2.5 nm and, when combined with polyethersulfone (PES) supports, the thinnest films of these COFs reject Rhodamine-WT (R-WT) dye and sodium chloride (NaCl) from water over broad pressure ranges. Banerjee and co-workers[22] synthesized β-ketoenamine-linked crystalline COF films via interfacial polymerization with a Brønsted acid at a liquid/liquid interface formed by slow diffusion. The films were relatively thick (2.1-5.3 μm) with pores around 25 Å and, when they were combined with a polyester non-woven porous support, rejected organic pollutants from water at 0.5 bar upstream pressure. These materials also exhibit high permeance towards organic solvents.[23] Lai,[24-25] Meng and Caro,[26] Li and Ma,[27] Liu and Wang[28], and Wei and Wang[29] have all recently published reports on the ability of COF membranes to reject and separate surrogates of organic pollutants. One of the singular promises of framework-based membranes is the ability to rationally vary the composition and functionality of their pores, yet there are no reports that correlate membrane rejection with systematic structural changes to the COF pore. Herein we report such a study by changing the effective pore size of an imine-linked COF film. These thin, free-standing films are incorporated into the TFC NF membrane structure prior to being tested for their ability to reject an organic pollutant surrogate and salt. The TFC NF membrane, consisting of a **TAPB-PDA-H** COF film on a polyacrylonitrile (PAN) support, exhibits comparable rejection to our previous studies but is more resistant to degradation in the presence of organic solvents. The modified **TAPB-PDA-R** COF membranes, which result from systematically decreasing the effective size of the COF pores upon incorporating either methyl or ethyl groups (**TAPB-PDA-Me** or **TAPB-PDA-Et** COF, respectively) show enhanced rejection of both R-WT and NaCl.

Prior to synthesizing combined COF membranes with different effective pore sizes, microcrystalline COF powders were synthesized from the corresponding monomers and characterized. We recently reported the synthesis of imine-linked COFs, including **TAPB-PDA-H**, using catalytic amounts of the Lewis acid $Sc(OTf)_3$ at room temperature.[30] Here we used identical reaction conditions to form **TAPB-PDA-Me** and **TAPB-PDA-Et** COF powders from 1,3,5-tris(4-aminophenyl)benzene (**TAPB**) and 2,5-disubstituted terephthalaldehyde monomers (**PDA-Me** or **PDA-Et**), which were prepared by adapting literature procedures (Scheme 1).[31] These COF powders were also synthesized by adapting typical AcOH-catalyzed polymerization conditions at elevated temperature[32] to ensure that the materials quality was not impeded by the methyl or ethyl substituents on the PDA monomers. Powder X-ray diffraction data (Figures S6-S9) indicate the COF powders formed via either synthetic method are crystalline, as judged by their higher order Bragg diffraction, including 100, 110, 200, 210, 220, 310, and 001 peaks. The average in-plane domain size for both **TAPB-PDA-Me** and **TAPB-PDA-Et** is calculated as 35 nm using the Le Bail Method. Porosimetry measurements for the COF powders synthesized with $Sc(OTf)_3$ (Figures S10-S11) exhibit type IV isotherms that do not completely level off prior to reaching the saturation pressure, and they show slight hysteresis effects upon desorption. COF powders synthesized with AcOH (S12-S13) exhibit typical type IV isotherms and level off for both **TAPB-PDA-Me** and **TAPB-PDA-Et** by 0.6 P/P_0. Interestingly, **TAPB-PDA-Me** levels off around 900 cm^3/g while **TAPB-PDA-Et** levels off around 870 cm^3/g, consistent with the size of the **TAPB-PDA-Et** pore being smaller than that of **TAPB-PDA-Me**. The pore width distribution for the powders formed under room temperature Lewis acid conditions (Figures S14-S15) was slightly larger than those for powders formed under elevated temperature Brønsted acid conditions (Figures S16-S17), but both routes produce materials with a smaller pore size for **TAPB-PDA-Et** than that for **TAPB-PDA-Me**. The calculated pore width for **TAPB-PDA-H** is 3.2 nm, which decreases to 3.0 nm and then 2.9 nm for **TAPB-PDA-Me** and **TAPB-PDA-Et**, respectively. The measured pore width distribution similarly shows a decrease in size from 3.3 nm to 3.2 nm from **TAPB-PDA-Me** to **TAPB-PDA-Et**. Brunauer-Emmett-Teller (BET) surface areas for **TAPB-PDA-Me** and **TAPB-PDA-Et** synthesized using either set of reaction conditions were 1800-1900 m^2/g at relative pressure (P/P_0) between 0.05-0.1, indicative of high-quality porous crystalline materials. It should be noted that the surface area for **TAPB-PDA-Me** (1830 m^2/g using $Sc(OTf)_3$ conditions, 1850 m^2/g using AcOH conditions) is similar to that of **TAPB-PDA-Et** (1870 m^2/g under $Sc(OTf)_3$ conditions, 1900 m^2/g under AcOH conditions), which matches the small increase calculated in Connolly surface areas between **TAPB-PDA-Me** and **TAPB-PDA-Et** (2450 m^2/g vs 2500 m^2/g, respectively). Elemental analyses for **TAPB-PDA-Me** and **TAPB-PDA-Et** powders formed using $Sc(OTf)_3$ correspond reasonably well to the expected elemental compositions.

Imine-linked COF thin films were subsequently synthesized using an analogous procedure to that used in our previous report.[21] **TAPB** and **PDA-H**, **PDA-Me**, or **PDA-Et** were dissolved in separate volumes of 4:1 dioxane:mesitylene, combined into a stock solution, and carefully layered on top of an aqueous solution containing the $Sc(OTf)_3$ catalyst. As seen previously,[20-21] film thickness could be controlled by altering the concentration or absolute volume of organic material polymerized (see SI). It should be noted that, unlike the combined **TAPB-PDA-H** stock solution which remained colorless for indefinite periods of time in the absence of catalyst, upon addition of **TAPB** to **PDA-Me** or **PDA-Et** at high concentrations, a yellow precipitate quickly formed even in the absence of the $Sc(OTf)_3$ catalyst. To minimize this background reactivity, solutions of **TAPB** and **PDA-Me** or **PDA-Et** were only combined into a stock solution immediately prior to membrane formation, and if the stock solution turned yellow or formed a precipitate then it was no longer used and a new, fresh stock solution was prepared (see SI).

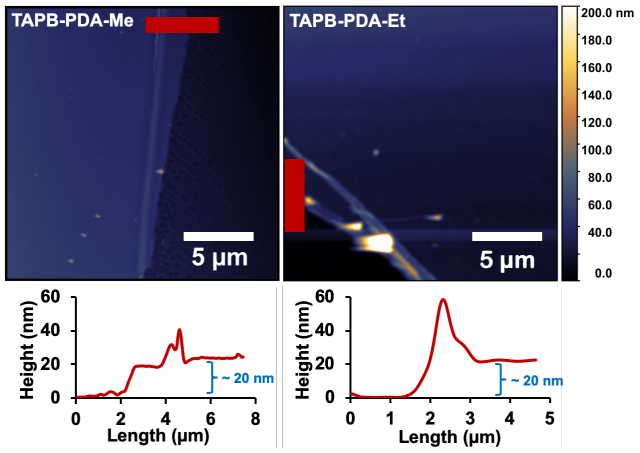

Figure 1. Atomic force microscopy (AFM) topography images of **TAPB-PDA-Me** film and **TAPB-PDA-Et** film. AFM height profile for corresponding film included under corresponding micrograph.

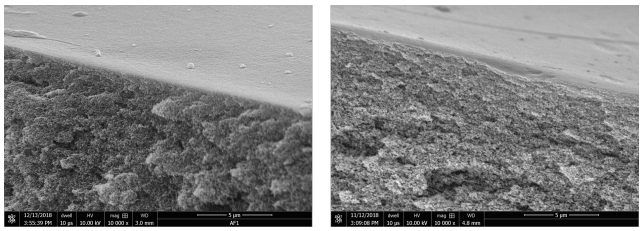

Figure 2. SEM cross-sectional image of thin-film composite PAN membrane containing **TAPB-PDA-Me** active layers (left). Control image of PAN membrane (right) included for comparison. Images were taken after membranes were exposed to organic solvent; no densification is observed. See Figures S23-30 for additional images.

The interfacially polymerized COF films were characterized by Fourier-transform infrared spectroscopy (FTIR), atomic force microscopy (AFM), optical microscopy, and grazing incidence wide angle X-ray scattering (GI-WAXS), which identified these materials as consistent with the formation of imine-linked networks. As expected of the vibrational data, the amine stretch of **TAPB** and the aldehyde stretch of **PDA-R** disappear upon condensation, and a new imine stretch appears for both the COF **TAPB-PDA-Me** and **TAPB-PDA-Et** powders and films (Figure S18). The resulting COF films are relatively large in dimension since we can alter the film coverage by changing the size of the polymerization interface (Figure S19). They have a thickness of approximately 20 nm (Figure 1) and are relatively smooth with a roughness of 3 nm and 6 nm for **TAPB-PDA-Me** and **TAPB-PDA-Et** films, respectively. The comparable film thicknesses indicate that the rates of polymerization were similar, so any differences in solute rejection tests could be associated to differences in COF pore size. We attempted GI-WAXS at the Advanced Photon Source at Argonne National Lab so as to obtain oriented crystallographic information about these films. While we cannot confirm crystallinity for **TAPB-PDA-H** (Figure S20), **TAPB-PDA-Me** (Figure S21), or **TAPB-PDA-Et** (Figure S22) films, studies by us[20] and others[25] indicate it is difficult to obtain confirmation of oriented crystallinity of COF films at this thickness. It is possible that we have synthesized a structure that: (a) is completely amorphous, (b) has local order but not long-range order (and/or lacks the regular stacking required for coherent diffraction), or (c) has long-range order but the accompanying diffraction signal is too weak to measure. Our previous studies[20-21] showed that thick films (100 μm) of **TAPB-PDA-H** are crystalline when prepared using this interfacial methodology, but they are too thick for performing membrane experiments. Instead we used thin films, despite their lack of observable diffraction, because they provide less resistance and therefore allow high water flux through the membrane at low energy inputs.

Thin-film composite membranes containing **TAPB-PDA-H**, **TAPB-PDA-Me**, or **TAPB-PDA-Et** active layers were synthesized and analyzed using scanning electron microscopy (SEM). A similar procedure was used as described previously,[20] in which free-standing imine-linked COF films were fabricated and transferred onto polyacrylonitrile (PAN) using Langmuir-Shaeffer techniques. The PAN was synthesized according to literature procedure[33] and chosen as the membrane support since it is resistant to decomposition in organic solvent. Previous work with **TAPB-PDA-H** thin-film COF membranes on a polyethersulfone (PES) support highlighted the incompatibility between the 1,4-dioxane:mesitylene solvent mixture required for the COF film synthesis and the PES material.[20] SEM images of the combined COF and PES membranes revealed the occurrence of PES densification after solvent exposure, which appeared to decrease the water permeability without affecting solute rejection of the combined membranes. The PAN used in this work did not undergo any appreciable densification upon solvent exposure, as seen in multiple SEM images (see Figures 2, S23-25 for cross-sectional images, and Figures S26-S30 for top-down images), and therefore was considered as a superior alternative.

TFC membranes of **TAPB-PDA-H**, **TAPB-PDA-Me**, or **TAPB-PDA-Et** on PAN were each tested for their water permeability and their ability to reject R-WT and NaCl, which are solutes used as surrogates for organic contaminants and background electrolytes, respectively. The solute rejection results are shown in Figure 3 with corresponding permeate fluxes shown in Figures 4 and S31-S32. These TFC membranes exhibit lower water permeability but enhanced R-WT and NaCl rejection when compared to the unmodified PAN support. We compared the performance of the TFC COF membranes to those of each PAN support before (pristine) and after (control) solvent exposure, as well as to the commercial nanofiltration membrane DOW FILMTEC NF-270. Solvent exposure did not affect membrane support performance, indicating that the COF film

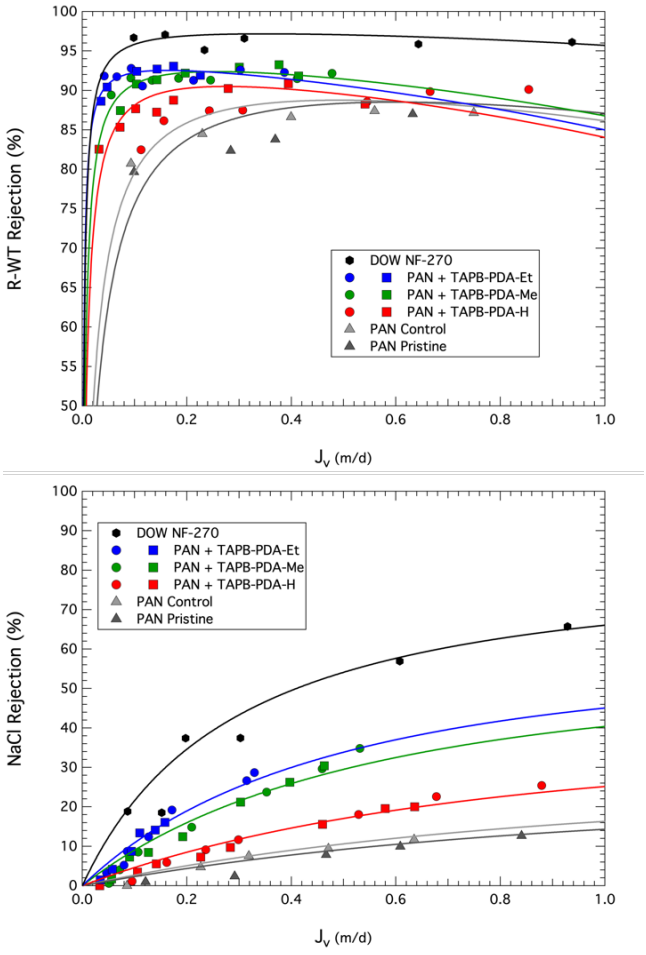

Figure 3. Rejection of surrogate organic contaminant Rhodamine-WT (R-WT) (upper plot) and representative electrolyte NaCl (lower plot) as a function of permeate flux J_v obtained for thin-film composite (TFC) polyacrylonitrile (PAN) membranes with COF active layers of **TAPB-PDA-H**, **TAPB-PDA-Me**, or **TAPB-PDA-Et**. Data also shown for corresponding pristine and control PAN supports without the COF active layer, and for commercial nanofiltration (NF) membrane (DOW FILMTEC NF-270).

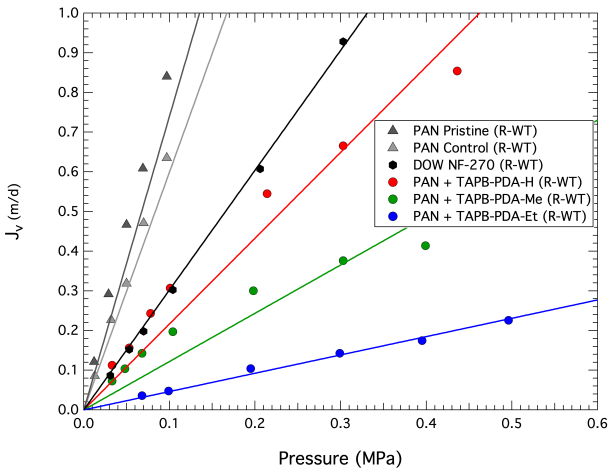

Figure 4. Permeate water flux J_v as a function of hydraulic pressure obtained for thin-film composite polyacrylonitrile (PAN) membranes with COF active layers of **TAPB-PDA-H**, **TAPB-PDA-Me**, or **TAPB-PDA-Et** tested with R-WT solutions (see Figure S31 for those tested with NaCl solutions and Figure S32 for combined regression lines). Data and regression lines are also shown for corresponding pristine and control PAN supports without the COF layer, and for commercial nanofiltration (NF) membrane (DOW FILMTEC NF-270).

itself plays an integral part in enhanced solute rejection. For example, at a low permeate water flux of 0.02 m/d, 49.0% of R-WT is rejected by the (control) PAN support, and rejection increases to 71.0%, 77.6%, or 86.2% upon addition of the **TAPB-PDA-H**, **TAPB-PDA-Me**, or **TAPB-PDA-Et** COF film, respectively. When the permeate water flux is increased to 0.1 m/d, R-WT rejection increases from 79.6% for the (control) PAN up to 88.1%, 90.8%, or 92.3% depending on the COF thin film added (**TAPB-PDA-H**, **TAPB-PDA-Me**, or **TAPB-PDA-Et**, respectively). It is critical to point out that increasing rejection at low pressure is very difficult since the diffusive transport of solutes through the membrane pores is more prevalent than at higher pressure for which higher advective transport takes place, and so these data best exhibit the differences between membrane materials. The R-WT rejection data shows hallmarks of separations associated with well-defined materials since there is increased rejection by the TFC COF membranes containing **TAPB-PDA-H** versus **TAPB-PDA-Me** versus **TAPB-PDA-Et** active layers. This trend is also seen in the NaCl rejection data. At a permeate water flux of 0.1 m/d, 2.71% of NaCl is rejected by the (control) PAN support, and rejection increased to 4.61%, 9.03%, or 10.9% upon addition of the **TAPB-PDA-H**, **TAPB-PDA-Me**, or **TAPB-PDA-Et** COF film, respectively. Even at a higher permeate water flux of 0.5 m/d, NaCl rejection increases from 10.6% for the (control) PAN support, up to 17.1%, 29.5%, or 33.9% upon addition of the **TAPB-PDA-H**, **TAPB-PDA-Me**, or **TAPB-PDA-Et** COF film, respectively. Thus, all of the COF membranes provide measurable, enhanced rejection of both R-WT and NaCl compared to the (control) PAN support and, furthermore, the data revealed a noticeable trend related to the type of **TAPB-PDA-R** used in the active layer: as the pendant group size increases from a hydrogen atom in **TAPB-PDA-H** to a methyl group in **TAPB-PDA-Me** and finally to an ethyl group in **TAPB-PDA-Et**, there is a systematic increase in rejection of both R-WT and NaCl.

The rejection data shown in Figures 3 and 4 were modeled using solution-diffusion model equations[20] and fit the experimental data points well. One of two equations were used to fit the data depending on whether a thin-film COF active layer was included in the membrane. The solute rejection data sets collected for pristine and control PAN shown in Figure 3 were fitted with the solution diffusion model (Eq. S1), which accounted for: solute diffusive permeation (B [m/d]), fraction of water flux passing through active layer imperfections (α [dimensionless]), solution mass transfer coefficient in concentration-polarization film (k [m/d]), and overall permeate flux (J_v [m/d]). Rejection data for both R-WT and NaCl were experimentally tested in duplicate for each of the TFC membranes containing a COF active layer (**TAPB-PDA-H**, **TAPB-PDA-Me**, and **TAPB-PDA-Et**), and they were combined and fitted with a modified two-film solution diffusion model (Eq. S2) to determine the intrinsic properties of the COF active layers separate from the PAN support.[20] The resulting fitted lines are depicted in Figure 3 and the corresponding fitting parameters are listed in Table 1, along with the water permeation coefficients (A [m/(d x MPa)]) obtained

Table 1. Water and solute transport parameters obtained by fitting the experimental data in Figures 3 and 4. Parameters B and α for R-WT and NaCl listed for the COF membranes are intrinsic transport parameters for the COF active layer obtained by fitting the corresponding data in Figure 3 with Equation S2 using the parameters obtained by fitting the solute rejection data for the control PAN support in Figure 3 with Equation S1. To observe comparable changes in B values for NaCl, the R-WT α value was used in NaCl modeling.

Membrane	R-WT			NaCl		
	A (m/d*MPa)	B (m/d)	α (-)	A (m/(d*MPa)	B (m/d)	α (-)
Pristine PAN	5.59 ± 0.18	0.026 ± 0.006	0.022 ± 0.011	7.39 ± 0.25	3.96 ± 0.28	0.022
Control PAN	6.39 ± 0.30	0.019 ± 0.003	0.032 ± 0.008	5.99 ± 0.19	3.35 ± 0.22	0.032
PAN + TAPB-PDA-H	2.16 ± 0.13	0.009 ± 0.002	0.065 ± 0.008	2.32 ± 0.10	3.66 ± 0.25	0.065
PAN + TAPB-PDA-Me	1.25 ± 0.06	0.006 ± 0.001	0.048 ± 0.004	1.47 ± 0.07	1.21 ± 0.08	0.048
PAN + TAPB-PDA-Et	0.91 ± 0.04	0.0021 ± 0.0004	0.055 ± 0.004	1.2 ± 0.4	0.92 ± 0.06	0.055
NF-270	3.06 ± 0.02	0.003 ± 0.001	0.012 ± 0.003	3.02 ± 0.01	0.35 ± 0.08	0.012

from the slopes of the plots in Figure 4. The mass transfer coefficients used in Equations S1 and S2 to represent concentration polarization of R-WT ($k_{R\text{-}WT}$ = 0.9 m/d) and NaCl (k_{NaCl} = 2.6 m/d) were obtained from previous analysis with these composite membranes.[20]

Additionally, there is a general decrease in permeate flux as the effective COF pore size decreases with increasing pendant group size. As the pendant groups grow in length, the overall hydrophobicity of the COF film also increases. A more hydrophobic membrane, together with a narrower pore, is consistent with reduced water permeability of the TFC COF membrane. We identified the same decrease in permeability with increasing **TAPB-PDA-H** COF thickness,[20] but we also observed no significant change in rejection capabilities. Greater pore constriction and increased hydrophobicity are consistent with the decreased TFC COF membrane permeate flux observed between the three membranes investigated here.

There is also a significant shift in the solute permeation coefficient (B) for the different TFC COF membranes (Table 1), which is consistent with the COF films presenting greater resistance to diffusive transport with an increasing molecular size of the pendant groups in the **TAPB-PDA-R** active layers. The change in the B parameter is likely due to increased tortuosity created by the pendant groups. The portion of solute transported through the COF active layer by pore surface diffusion is affected by the molecular size of the pendant groups branching into the COF pores. The pendant groups create obstacles, which slow down the surface diffusion capability and increase the rejection of the solute. In contrast, corresponding changes in the advective transport parameter, α, are small, supporting the slight change the **TAPB-PDA-R** pendant groups have on the COF pore size.

It is also important to note the comparison between the TFC **TAPB-PDA-H** PAN membranes investigated here and the TFC **TAPB-PDA-H** PES membrane evaluated previously.[20-21] Although two different support materials were used, the two-film solution diffusion model (Eq. S2) provided values that are statistically similar when evaluated using a t-test (two-tail distribution, equal variance) for the R-WT data sets (B=0.009 ± 0.002 in the present study and B=0.012 ± 0.002 m/d in the previous study[20]). This confirms that the **TAPB-PDA-H** active layer formed in both studies on different supports are similar. Unfortunately, a direct comparison between the NaCl data sets was more difficult because the low rejection observed for NaCl does not allow for accurate differentiation between diffusive and advective transport. As Figures 3 and 4 show, the permeate flux and solute rejection by all COF membranes were lower than those observed for the NF-270 commercial membrane. Decreasing the COF pore size and using supports with higher permeate flux should help to address these differences.

In conclusion, we have developed an interfacial polymerization method to probe thin layers of COF films or related cross-linked networks and incorporated them into TFC membranes with a PAN support. Although these materials do not show evidence of long-range order, their rejection behavior exhibits characteristics associated with a progressive decrease in pore size as the pendant group length in the COF active layer is increased from hydrogen to methyl to ethyl. There is also a significant shift in the solute permeation coefficient, B, consistent with the COF films presenting greater resistance to diffusive transport with decreasing COF pore size and increasing pendant group length. These results indicate that rational changes can be correlated to membrane performance, even in materials with no observable long-range order. As methods to access extremely thin COF films with unambiguous long-range order (perhaps even as single or few-layer structures) are developed, these results represent an important benchmark towards the importance of structural design and membrane performance.

ASSOCIATED CONTENT

Supporting Information

The Supporting Information is available free of charge on the ChemRxiv website:

Materials and instrumentation; experimental procedures and characterizations; ^{1}H and ^{13}C NMR spectra of COF monomers; powder X-ray diffraction patterns of COF powders; nitrogen adsorption isotherms and BET plots for COF powders; pore distributions for COF powders; vibrational data for COF monomers, powders, and films; optical microscopy images of COF films; grazing incidence wide angle X-ray scattering (GI-WAXS) patterns of COF films; SEM images of TFC COF PAN membranes; solution-diffusion model equations; and permeate water flux as a function of hydraulic pressure (PDF).

AUTHOR INFORMATION

Corresponding Author

*WRD: wdichtel@northwestern.edu

Author Contributions

‡A.R.C. and G.A.L. contributed equally.

Notes

The authors declare no competing financial interests.

ACKNOWLEDGMENT

This research was supported by the National Science Foundation (CBET-1706219) and used resources at the Advanced Photon Source (Sector 8), which is a Department of Energy Office of Science User Facility (DE-AC02-05CH11231). A.M.E. is supported by an NSF Graduate Research Fellowship (DGE-1324585). The UK based team was supported by the Engineering and Physical Sciences Research Council (CBET-EPSRC EP/R018847).

REFERENCES

1. *The United Nations World Water Development Report 2019: Leaving No One Behind*; UNESCO: 2019.
2. Elimelech, M.; Phillip, W. A., The Future of Seawater Desalination: Energy, Technology, and the Environment. *Science* **2011,** *333* (6043), 712.
3. Colson, J. W.; Dichtel, W. R., Rationally synthesized two-dimensional polymers. *Nat. Chem.* **2013,** *5* (6), 453-65.
4. DeBlase, C. R.; Dichtel, W. R., Moving Beyond Boron: The Emergence of New Linkage Chemistries in Covalent Organic Frameworks. *Macromolecules* **2016,** *49* (15), 5297-5305.
5. Bisbey, R. P.; Dichtel, W. R., Covalent Organic Frameworks as a Platform for Multidimensional Polymerization. *ACS Cent. Sci.* **2017,** *3* (6), 533-543.
6. Diercks, C. S.; Yaghi, O. M., The atom, the molecule, and the covalent organic framework. *Science* **2017,** *355* (6328), 923.
7. Jin, Y.; Hu, Y.; Zhang, W., Tessellated multiporous two-dimensional covalent organic frameworks. *Nat. Rev. Chem.* **2017,** *1*, 0056.
8. Lohse, M. S.; Bein, T., Covalent Organic Frameworks: Structures, Synthesis, and Applications. *Adv. Funct. Mater.* **2018,** *28* (33), 1705553.
9. Kandambeth, S.; Dey, K.; Banerjee, R., Covalent Organic Frameworks: Chemistry beyond the Structure. *J. Am. Chem. Soc.* **2019,** *141* (5), 1807-1822.

10. Song, Y.; Sun, Q.; Aguila, B.; Ma, S., Opportunities of Covalent Organic Frameworks for Advanced Applications. *Adv. Sci.* **2019,** *6* (2), 1801410.

11. Colson, J. W.; Woll, A. R.; Mukherjee, A.; Levendorf, M. P.; Spitler, E. L.; Shields, V. B.; Spencer, M. G.; Park, J.; Dichtel, W. R., Oriented 2D covalent organic framework thin films on single-layer graphene. *Science* **2011,** *332* (6026), 228-31.

12. Kim, S.; Lim, H.; Lee, J.; Choi, H. C., Synthesis of a Scalable Two-Dimensional Covalent Organic Framework by the Photon-Assisted Imine Condensation Reaction on the Water Surface. *Langmuir* **2018,** *34* (30), 8731-8738.

13. Karak, S.; Kandambeth, S.; Biswal, B. P.; Sasmal, H. S.; Kumar, S.; Pachfule, P.; Banerjee, R., Constructing Ultraporous Covalent Organic Frameworks in Seconds via an Organic Terracotta Process. *J. Am. Chem. Soc.* **2017,** *139* (5), 1856-1862.

14. Smith, B. J.; Parent, L. R.; Overholts, A. C.; Beaucage, P. A.; Bisbey, R. P.; Chavez, A. D.; Hwang, N.; Park, C.; Evans, A. M.; Gianneschi, N. C.; Dichtel, W. R., Colloidal Covalent Organic Frameworks. *ACS Cent. Sci.* **2017,** *3* (1), 58-65.

15. Evans, A. M.; Parent, L. R.; Flanders, N. C.; Bisbey, R. P.; Vitaku, E.; Chen, L. X.; Gianneschi, N. C.; Dichtel, W. R., Seeded growth of single-crystal two-dimensional covalent organic frameworks. *Science* **2018,** *361* (6397), 52-57.

16. Li, R. L.; Flanders, N. C.; Evans, A. M.; Ji, W.; Castano, I.; Chen, L. X.; Gianneschi, N. C.; Dichtel, W. R., Controlled growth of imine-linked two-dimensional covalent organic framework nanoparticles. *Chem. Sci.* **2019,** *10* (13), 3796-3801.

17. Fernandes, S. P. S.; Romero, V.; Espiña, B.; Salonen, L. M., Tailoring Covalent Organic Frameworks to Capture Water Contaminants. *Chem. Eur. J.* **2019,** *25* (26), 6461-6473.

18. Wang, H.; Zeng, Z.; Xu, P.; Li, L.; Zeng, G.; Xiao, R.; Tang, Z.; Huang, D.; Tang, L.; Lai, C.; Jiang, D.; Liu, Y.; Yi, H.; Qin, L.; Ye, S.; Ren, X.; Tang, W., Recent progress in covalent organic framework thin films: fabrications, applications and perspectives. *Chem. Soc. Rev.* **2019,** *48* (2), 488-516.

19. Yuan, S.; Li, X.; Zhu, J.; Zhang, G.; Van Puyvelde, P.; Van der Bruggen, B., Covalent Organic Frameworks for Membrane Separation. *Chem. Soc. Rev.* **2019**.

20. Valentino, L.; Matsumoto, M.; Dichtel, W. R.; Marinas, B. J., Development and Performance Characterization of a Polyimine Covalent Organic Framework Thin-Film Composite Nanofiltration Membrane. *Environ. Sci. Technol.* **2017,** *51* (24), 14352-14359.

21. Matsumoto, M.; Valentino, L.; Stiehl, G. M.; Balch, H. B.; Corcos, A. R.; Wang, F.; Ralph, D. C.; Marinas, B. J.; Dichtel, W. R., Lewis-Acid-Catalyzed Interfacial Polymerization of Covalent Organic Framework Films. *Chem* **2018,** *4* (2), 308-317.

22. Dey, K.; Pal, M.; Rout, K. C.; Kunjattu, H. S.; Das, A.; Mukherjee, R.; Kharul, U. K.; Banerjee, R., Selective Molecular Separation by Interfacially Crystallized Covalent Organic Framework Thin Films. *J. Am. Chem. Soc.* **2017,** *139* (37), 13083-13091.

23. Kandambeth, S.; Biswal, B. P.; Chaudhari, H. D.; Rout, K. C.; Kunjattu, H. S.; Mitra, S.; Karak, S.; Das, A.; Mukherjee, R.; Kharul, U. K.; Banerjee, R., Selective Molecular Sieving in Self-Standing Porous Covalent-Organic-Framework Membranes. *Adv. Mater.* **2017,** *29* (2), 1603945.

24. Gadwal, I.; Sheng, G.; Thankamony, R. L.; Liu, Y.; Li, H.; Lai, Z., Synthesis of Sub-10 nm Two-Dimensional Covalent Organic Thin Film with Sharp Molecular Sieving Nanofiltration. *ACS Appl. Mater. Interfaces.* **2018,** *10* (15), 12295-12299.

25. Shinde, D. B.; Sheng, G.; Li, X.; Ostwal, M.; Emwas, A. H.; Huang, K. W.; Lai, Z., Crystalline 2D Covalent Organic Framework Membranes for High-Flux Organic Solvent Nanofiltration. *J. Am. Chem. Soc.* **2018,** *140* (43), 14342-14349.

26. Fan, H.; Gu, J.; Meng, H.; Knebel, A.; Caro, J., High-Flux Membranes Based on the Covalent Organic Framework COF-LZU1 for Selective Dye Separation by Nanofiltration. *Angew. Chem., Int. Ed.* **2018,** *57* (15), 4083-4087.

27. Zhang, W.; Zhang, L.; Zhao, H.; Li, B.; Ma, H., A two-dimensional cationic covalent organic framework membrane for selective molecular sieving. *J. Mater. Chem. A* **2018,** *6* (27), 13331-13339.

28. Hao, Q.; Zhao, C.; Sun, B.; Lu, C.; Liu, J.; Liu, M.; Wan, L.-J.; Wang, D., Confined Synthesis of Two-Dimensional Covalent Organic Framework Thin Films within Superspreading Water Layer. *J. Am. Chem. Soc.* **2018,** *140* (38), 12152-12158.

29. Zhou, W.; Wei, M.; Zhang, X.; Xu, F.; Wang, Y., Fast Desalination by Multilayered Covalent Organic Framework (COF) Nanosheets. *ACS Appl. Mater. Interfaces* **2019,** *11* (18), 16847-16854.

30. Matsumoto, M.; Dasari, R. R.; Ji, W.; Feriante, C. H.; Parker, T. C.; Marder, S. R.; Dichtel, W. R., Rapid, Low Temperature Formation of Imine-Linked Covalent Organic Frameworks Catalyzed by Metal Triflates. *J. Am. Chem. Soc.* **2017,** *139* (14), 4999-5002.

31. Wessig, P.; Gerngroß, M.; Freyse, D.; Bruhns, P.; Przezdziak, M.; Schilde, U.; Kelling, A., Molecular Rods Based on Oligo-spiro-thioketals. *J. Org. Chem.* **2016,** *81* (3), 1125-1136.

32. Smith, B. J.; Overholts, A. C.; Hwang, N.; Dichtel, W. R., Insight into the crystallization of amorphous imine-linked polymer networks to 2D covalent organic frameworks. *Chem. Commun.* **2016,** *52* (18), 3690-3693.

33. Cook, M.; Gaffney, P. R. J.; Peeva, L. G.; Livingston, A. G., Roll-to-roll dip coating of three different PIMs for Organic Solvent Nanofiltration. *J. Membrane Sci.* **2018,** *558*, 52-63.

Table of Contents Image

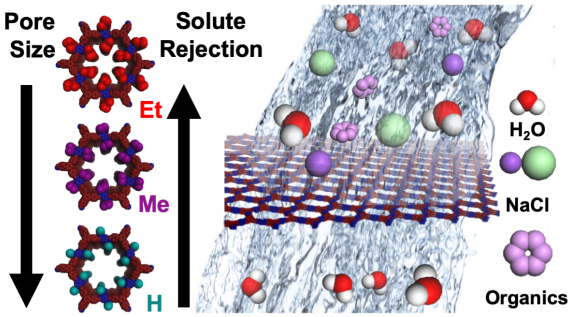

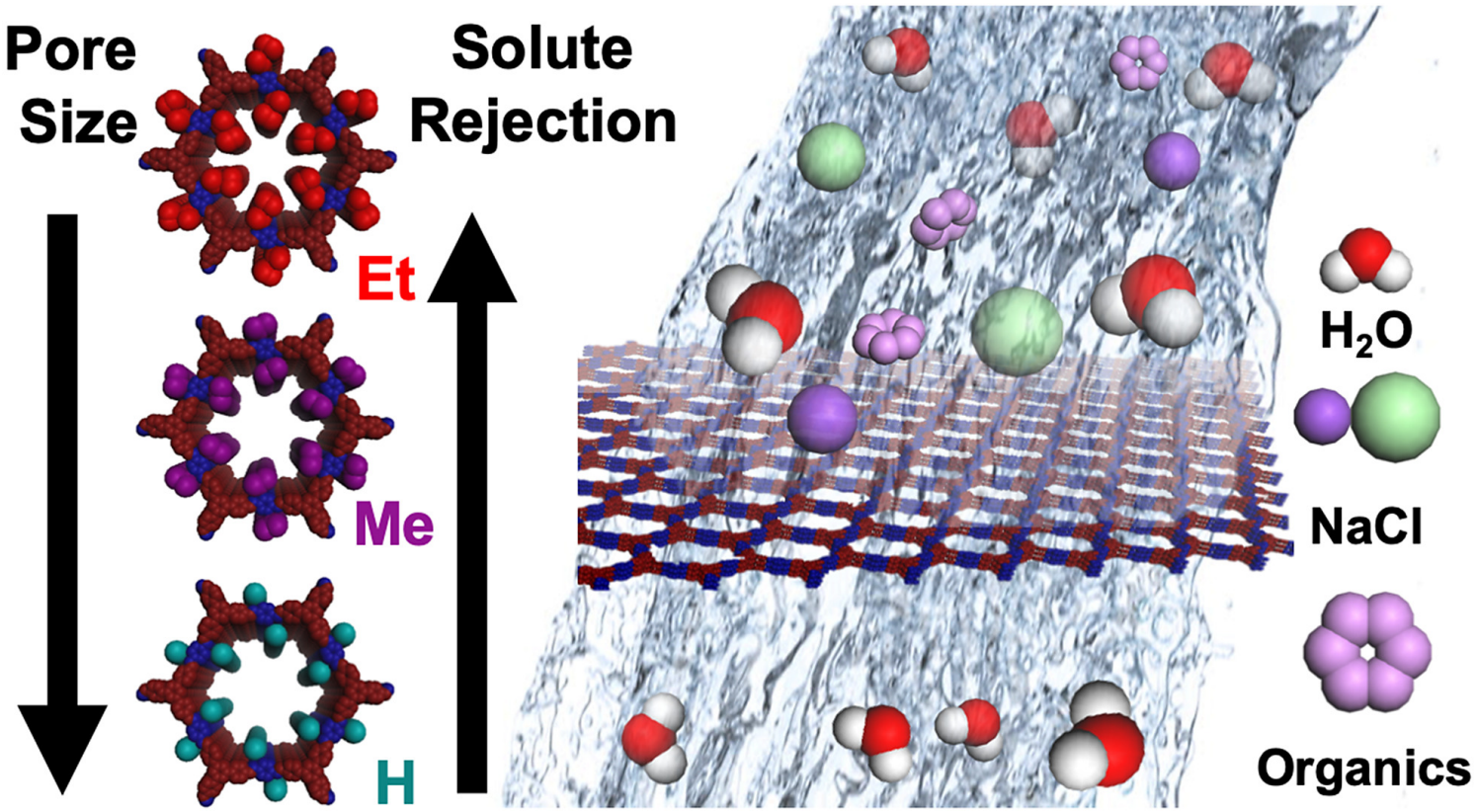

2019_07_ChemRxiv_Corcos_TOC.tif (4.15 MiB) view on ChemRxiv • download file

Reducing the Pore Size of Covalent Organic Frameworks in Thin-Film Composite Membranes Enhances Solute Rejection

Amanda R. Corcos,[1,†] Gabrielle A. Levato,[2,†] Zhiwei Jiang,[3] Austin M. Evans,[1] Andrew G. Livingston,[3] Benito J. Mariñas,[2] and William R. Dichtel[1,*]

[1]*Department of Chemistry, Northwestern University, 2145 Sheridan Road, Evanston, Illinois 60208, United States*

[2]*Safe Global Water Institute, Department of Civil and Environmental Engineering, University of Illinois at Urbana-Champaign, Urbana, Illinois 61801, United States*

[3]*Barrer Centre, Department of Chemical Engineering, Imperial College London, South Kensington Campus, Exhibition Road, London SW7 2AZ, United Kingdom*

Supplementary Information

Correspondence Address

Professor William R. Dichtel
Department of Chemistry
Northwestern University
2145 Sheridan Road
Evanston, IL 60208 (USA)
wdichtel@northwestern.edu

Table of Contents

A. Materials and Instrumentation S-2
B. Synthetic Procedures and Characterizations S-6
C. ^{1}H and ^{13}C NMR Spectra of COF Monomers S-12
D. Powder X-ray Diffraction Patterns for COF Powders S-14
E. Nitrogen Adsorption Isotherms and BET Plots for COF Powders S-16
F. Pore Distributions for COF Powders S-18
G. Vibrational Data for COF Monomers, Powders, and Films S-20
H. Optical Microscopy of COF Films S-20
I. Grazing Incidence Wide Angle X-ray Scattering (GI-WAX) of COF Films S-21
J. SEM Images of Thin-Film Composite COF PAN Membranes S-22
K. Solution-Diffusion Model Equations S-25
L. Permeate Water Flux as a Function of Hydraulic Pressure S-26
M. References S-27

A. Materials and Instrumentation.

Materials.

Reagents were purchased in reagent grade from commercial suppliers and used without further purification, unless otherwise described. Anhydrous solvents (CH_2Cl_2, DMF, THF, CH_3CN, toluene, CH_3OH) were obtained from a solvent purification system (JC Myer System). 2,5-dimethylbenzene-1,4-dicarboxaldehyde (**PDA-Me**) and 2,5-diethylbenzene-1,4-dicarboxaldehyde (**PDA-Et**) were prepared by adapting literature procedures.[1] Polyacrilonitrile (PAN) membranes were prepared according to literature procedure.[2]

Instrumentation.

Infrared Spectroscopy. Infrared spectra were recorded on a Nicolet iS10 FT-IR spectrometer equipped with a ZnSe ATR attachment and are uncorrected.

Nuclear Magnetic Resonance. Proton and carbon nuclear magnetic resonance (NMR) spectra were recorded at 25 °C on a Bruker Avance III 500 MHz spectrometer. The spectra were calibrated using residual solvent as an internal reference ($CDCl_3$: 7.26 ppm for ^1H NMR, 77.16 for ^{13}C NMR).

High Resolution Mass Spectrometry. High resolution mass spectra were acquired on an Agilent 6210A LC-TOF mass spectrometer with an Atmospheric Pressure Photoionization (APPI) source. The instrument was equipped with an Agilent Series 1200 HPLC binary pump and an autosampler which used Mass Hunter software. The samples were evaluated using direct injection.

Elemental Analysis. Elemental analyses were performed on an Elementar Vario Cube EL CHNS elemental analyzer by the Integrated Molecular Structure Education and Research Center (IMSERC) at Northwestern University.

Critical Point Dryer. Drying of samples using supercritical CO_2 was performed in a Leica EM 300 critical point dryer. Prior to the supercritical drying process, all samples were placed in tea bags (ETS Drawstring Tea Filters, sold by English Tea Store) while wet and then subjected to CH_3OH Soxhlet procedures. The tea bags containing the samples were then placed in the drying chamber. The chamber was sealed, cooled to 15 °C, quickly filled with liquid CO_2, and then vented. This fill-vent cycle was repeated 55 times, after which the temperature was raised to 45 °C, resulting in a chamber pressure above the critical point of CO_2. The chamber pressure was slowly released.

Powder X-ray Diffraction. Powder X-ray diffraction (PXRD) patters were obtained at room temperature on a STOE-STADIP powder diffractometer equipped with an asymmetric curved Germanium monochromator. (Cu-Kα radiation, λ = 1.54056 Å) and one-dimensional silicon strip detector (MYTHEN2 1K from DECTRIS). The line focused Cu X-ray tube was operated at 40 kV and 40 mA. The as-obtained powder samples were sandwiched between two acetate foils (polymer sample with neither Bragg reflections nor broad peaks above 10° 2θ) mounted in flat plates with a disc opening diameter of 8 mm and measured in transmission geometry in a rotating holder. The patterns were recorded in the 2θ range of 0-36° for an overall exposure time of 25 min. The instrument was calibrated against a NIST Silicon standard (640d) prior to the measurement.

Gas Adsorption. Gas adsorption isotherms were performed on a Micromeritics ASAP 2420 Accelerated Surface Area and Porosity Analyzer using 20-30 mg samples in dried and tared analysis tubes that were capped with a Transeal. UHP-grade (99.999% purity) N_2 was used for all adsorption measurements. N_2 isotherms were generated by incremental exposure to nitrogen up to 760 mmHg (1 atm) in liquid nitrogen (77 K) bath. Oil-free vacuum pumps and oil-free pressure regulators were used for all measurements. Branauer-Emmett-Teller (BET) surface areas were calculated from the linear region of the N_2 isotherm at 77 K within the pressure range P/P_0 of 0.05-0.10.

Atomic Force Microscopy and Optical Microscopy. Atomic force microscopy (AFM) data and optical microscopy images were collected on a Bruker Dimension FastScan® Atomic Force Microscope.

Scanning Electron Microscopy. Scanning electron microscopy (SEM) data were collected on a FEI Quanta 450 FEG microscope (FEI, Hillsboro, OR) at the Beckman Institute for Advanced Scient and Technology and the University of Illinois at Urbana-Champaign. Prior to analysis, membranes were attached to an aluminum stand with carbon tape and sputter coated with Au/Pd for 70 seconds.

Sonication. Sonication was performed with a Branson 3510 ultrasonic cleaner with a power output of 100 W and a frequency of 42 kHz.

Grazing Incidence Wide-Angle X-ray Scattering. Grazing incidence wide-angle X-ray scattering (GI-WAXS) experiments were performed at Sector 8-ID-E of Argonne National Laboratory at an energy of 11 keV. Samples were mounted as prepared on SiO_2 substrates and put under vacuum. Incidence angles of ~0.14° were aligned and exposures were timed such that the highest count pixels were 80% of their maximum.

Permeation Experiments. Permeation experiments were conducted using a dead-end stirred cell (Amicon model 8010, EMD Millipore, Billerica, MA) at room temperature. Feed solutions (2.5 mg/L of Rhodamine-WT (R-WT) and 400 mg/L of NaCl) were prepared by dilution of a concentrated solution (R-WT: 20% w/w, Turner Designs, San Jose, CA; NaCl: 99%, EMD Millipore, Darmstadt, Germany). The feed solution pH was adjusted to 6.75 ± 0.1 using HCl or NaOH aqueous solutions prior to each experiment. Permeate flow rates were measured gravimetrically, and the data were recorded using a balance connected to a computer with data acquisition software. Experiments were performed over a range of pressures from 0.01-0.4 MPa using nitrogen gas as the pressure source. Rhodamine-WT concentrations were determined using a spectrofluorometer (RF-5301PC, Shimadzu Scientific Instruments Inc., Columbia, MD) with an excitation wavelength of 550 and emission wavelength of 580 nm. NaCl concentrations were determined using an ion chromatograph (ICS-2100, Dionex, Sunnyvale, CA) with 4 mm IonPac AS18 analytical and AG18 guard columns, 23 mM KOH eluent, 57 mA suppressor current, flow rate of 1 mL/min, and a 25 μL sample loop and injection volume.

B. Synthetic Procedures and Characterizations

Scheme S1.

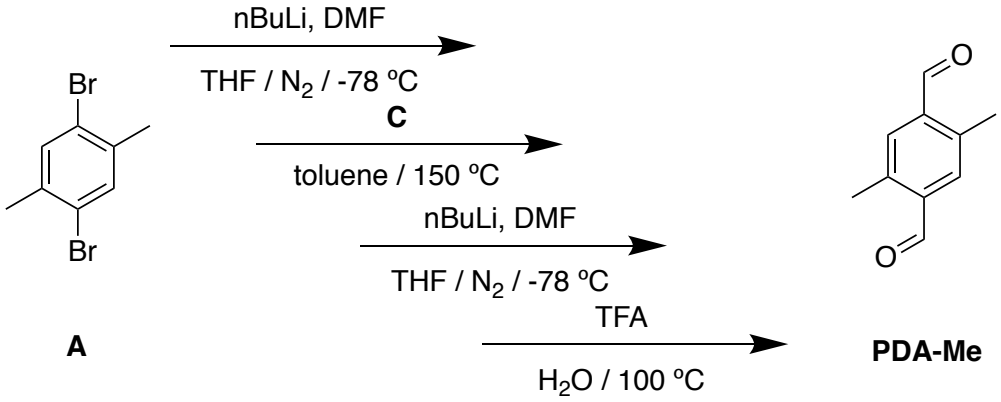

Synthesis of 2,5-dimethylbenzene-1,4-dicarboxaldehyde (PDA-Me): This compound was synthesized according to published procedure with minor modifications.[1] In a Schlenk flask, 1,4-dibromo-2,5-dimethylbenzene (**A**, 18.00 g, 68.19 mmol) was dissolved in dry THF (200 mL) under N_2 and cooled to -78 °C. *n*BuLi (2.5 M in hexanes, 30 mL, 75.0 mmol) was added dropwise via cannula. The mixture was allowed to stir at -78 °C for 15 min before dry DMF (11 mL) was added. The reaction was allowed to warm to rt while stirring for 2 h, after which it was charged with concentrated HCl. The mixture was extracted with Et_2O two times, and the combined organic layers were washed with brine, dried over $MgSO_4$, and concentrated under reduced pressure. The residue was used without further purification and was refluxed overnight in a Dean-Stark apparatus with toluene (130 mL), neopentyl glycol (**C**, 14.2 g), and p-TsOH (2.42 g). The mixture was washed with a saturated $NaHCO_3$ solution, water, brine, and dried over $MgSO_4$ before concentration under reduced pressure. The residue was treated a second time as described above with the same amounts of *n*BuLi and DMF under the same conditions (the protection using neopentyl glycol was not repeated). After isolation, the product was refluxed in water (16 mL) and TFA (120 mL) for 15 min. The mixture was concentrated under reduced pressure and charged with

CH_2Cl_2. It was then washed with saturated $NaHCO_3$ solution, brined, dried over $MgSO_4$, and concentrated under reduced pressure. The resulting liquid (which was a saturated solution of **PDA-Me** in residual DMF) was placed in a freezer overnight. The resulting **PDA-Me** precipitate was isolated via filtration and washed with hexanes. Isolated yield of **PDA-Me**: 3.34 g (30.2%). NMR shifts for this compound were consistent with those previously reported.[1] ^{1}H NMR (500 MHz, $CDCl_3$) δ 10.33 (s, 2H), 7.69 (s, 2H), 2.69 (s, 6H) ppm. ^{13}C NMR (125 MHz, $CDCl_3$) δ 192.34, 138.30, 137.06, 134.84, 18.95 ppm. IR (solid, ATR) 3355, 2979, 2910, 2788, 1787, 1679, 1651, 1595. 1558, 1489, 1461, 1441, 1393, 1384, 1347, 1290, 1219, 1161, 1080, 1041, 998, 965, 894, 864, 776, 723, 701, 664 cm^{-1}. Elemental analysis: Theoretical C 74.06 H 6.22; Found C 70.19 H 6.16. HRMS calculated for $[C_{10}H_{10}O_2H]^+$ 163.0754, found 163.0758.

Scheme S2.

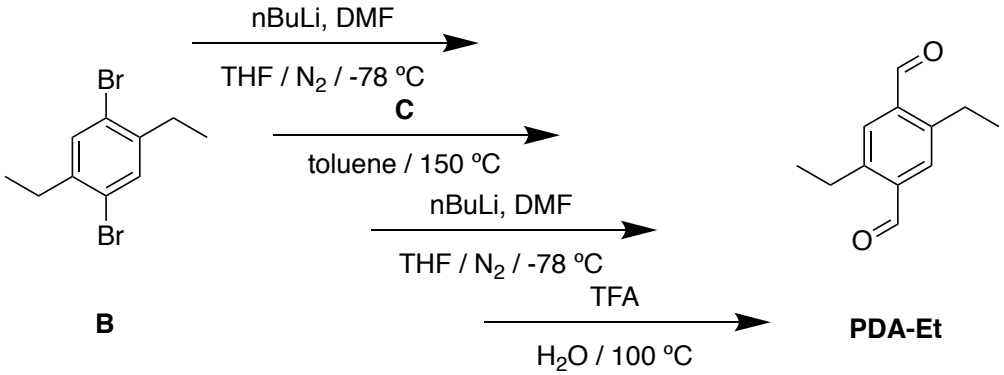

Synthesis of 2,5-diethylbenzene-1,4-dicarboxaldehyde (PDA-Et): This compound was synthesized by adapting the published procedure[1] for PDA-Me. In a Schlenk flask, 1,4-dibromo-2,5-diethylbenzene (**B**, 10.00 g, 34.2 mmol) was dissolved in dry THF (100 mL) under N_2 and cooled to -78 °C. *n*BuLi (2.5 M in hexanes, 15 mL, 37.5 mmol) was added dropwise via cannula. The mixture was allowed to stir at -78 °C for 15 min before dry DMF (6 mL) was added. The reaction was allowed to warm to rt while stirring for 2 h, after which it was charged with

concentrated HCl. The mixture was extracted with Et_2O two times, and the combined organic layers were washed with brine, dried over $MgSO_4$, and concentrated under reduced pressure. The residue was used without further purification and was refluxed overnight in a Dean-Stark apparatus with toluene (65 mL), neopentyl glycol (**C**, 7.13 g), and p-TsOH (1.21 g). The mixture was washed with a saturated $NaHCO_3$ solution, water, brine, and dried over $MgSO_4$ before concentration under reduced pressure. The residue was treated a second time as described above with the same amounts of *n*BuLi and DMF under the same conditions (the protection using neopentyl glycol was not repeated). After isolation, the product was refluxed in water (8 mL) and TFA (65 mL) for 15 min. The mixture was concentrated under reduced pressure and charged with CH_2Cl_2. It was then washed with saturated $NaHCO_3$ solution, brined, dried over $MgSO_4$, and concentrated under reduced pressure. The resulting liquid (which was a saturated solution of **PDA-Et** in residual DMF) was placed in a freezer overnight. The resulting **PDA-Et** precipitate was isolated via filtration and washed with hexanes. Isolated yield of **PDA-Et**: 1.98 g (30.4%). ^{1}H NMR (500 MHz, $CDCl_3$) δ 10.36 (s, 2H), 7.75 (s, 2H), 3.10 (q, 4H), 1.30 (t, 6H) ppm. ^{13}C NMR (125 MHz, $CDCl_3$) δ 191.92, 144.73, 136.87, 132.93, 25.19, 16.35 ppm. IR (solid, ATR) 3350, 2965, 2876, 2772, 1785, 1677, 1487, 1472, 1154, 1401, 1309, 1238, 1178, 1157, 1065, 1001, 972, 906, 847, 785, 679 cm^{-1}. Elemental analysis: Theoretical C 75.76 H 7.42; Found C 74.75 H 7.51. HRMS calculated for $[C_{12}H_{14}O_2Na]^+$ 213.0886, found 213.0893.

COF Powder General Reaction Procedure with $Sc(OTf)_3$: This procedure is based on a published procedure with minor modification.[3] In separate scintillation vials, 1,3,5-tris(4-aminophenyl)benzene (35.1 mg, 0.100 mmol) and aldehyde of choice (0.150 mmol, 1.5 eq.) were each dissolved in a 1,4-dioxane:mesitylene solution (4:1 v/v, 2 mL) and heated to 70 °C. Both

solutions were cooled to room temperature, and the amine-containing solution was then added to the aldehyde containing solution. The $Sc(OTf)_3$ catalyst (3.6 mg, 0.0073 mmol, 0.022 eq) was immediately added, the solution underwent sonication for 30 seconds, and the mixture was then allowed to stand on the benchtop for 3 hr. The resulting COF powder was transferred to a tea bag, washed with a 1,4-dioxane:mesitylene solution (4:1 v/v), and then washed with MeOH in a Soxhlet extractor for 18 hrs. The material was then dried by supercritical CO_2 to afford a yellow powder. **TAPB-PDA-Me**: Isolated yield 41.1 mg (75.7%). IR (solid, ATR) 3361, 3033, 2926, 1694, 1620, 1594, 1548, 1505, 1444, 1406, 1318, 1185, 1110, 1077, 1037, 1013, 970, 898, 828, 774, 731, 700 cm^{-1}. Elemental analysis: Theoretical C 86.64 H 5.59 N 7.77; Found C 84.64 H 5.49 N 7.68. **TAPB-PDA-Et**: Isolated yield 50.9 mg (87.2%). IR (solid, ATR) 3354, 3033, 2965, 1695, 1621, 1594, 1547, 1505, 1444, 1413, 1318, 1246, 1182, 1158, 1108, 1076, 1061, 1013, 970, 901, 828, 732, 706 cm^{-1}. Elemental analysis: Theoretical C 86.56 H 6.23 N 7.21; Found C 84.87 H 6.20 N 7.26.

COF Powder General Reaction Procedure with AcOH: This procedure is based on a published procedure with minor modification.[4] In separate scintillation vials, 1,3,5-tris(4-aminophenyl)benzene (175.5 mg, 0.500 mmol) and aldehyde of choice (0.750 mmol, 1.5 eq.) were each dissolved in a 1,4-dioxane:mesitylene solution (4:1 v/v, 10 mL). Due to a lack of solubility, the amine-containing solution was heated to 70 °C. Once the monomer was dissolved, the solution was cooled to room temperature, and the aldehyde-containing solution was added to the amine-containing solution. Glacial acetic acid (4.5 mL) was combined with deionized water (3.0 mL) and then immediately added to the solution, whereupon a precipitate began the form. The mixture was allowed to heat in an oven for 96 hr at 70 °C. The resulting COF powder was transferred to a tea

bag, washed with a 1,4-dioxane:mesitylene solution (4:1 v/v), and then washed with MeOH in a Soxhlet extractor for 18 hrs. The material was then dried by supercritical CO_2 to afford a yellow powder, which was further dried under vacuum for 12 hrs. **TAPB-PDA-Me**: Isolated yield 183.4 mg (67.9%). **TAPB-PDA-Et**: Isolated yield 187.6 mg (64.5%).

COF Film General Reaction Procedure: This procedure is based on a published procedure with minor modification.[5-6] A 5 mM aqueous solution of $Sc(OTf)_3$ was prepared by dissolving 24.7 mg of $Sc(OTf)_3$ in 10 mL of deionized water. In separate 20 mL scintillation vials, 1,3,5-tris(4-aminophenyl)benzene (12.3 mg, 0.0350 mmol) and aldehyde of choice (0.0525 mmol, 1.5 eq.) were each dissolved in a 1,4-dioxane:mesitylene solution (4:1 v/v, 5.6 mL) and heated to 70 °C. Once the monomers were dissolved, the solutions were cooled to room temperature, and the amine-containing solution was then added to the aldehyde containing solution. 40 uL of this combined organic solution (3.125 mM TAPB, 4.688 mL aldehyde) was then layered on top of 2.0 mL of the aqueous catalyst-containing solution in a 20 mL vial and allowed to sit at room temperature for 30 min. During this time, a film formed at the interface between the organic and aqueous layers. This grown film was transferred onto a substrate by inserting the substrate underneath the interface and lifting the substrate up slowly, after which the film was allowed to dry in air.

COF Films on Top of PAN Support Membranes: For the interfacial polymerization of a COF film and its transfer to a supporting PAN membrane, the membrane holder component of a dead-end filtration cell (Amicon 8010 series, EMD Millipore, Billerica, MA) was repurposed for the reactor. The PAN substrate was placed at the bottom of the reactor, and the interfacial

polymerization was designed to take place above the PAN support. This procedure is based on a published procedure with minor modification.[5-6]

A stock solution of monomers was prepared by combining TAPB (8.8 mg, 1.56 mM) and aldehyde of choice (2.34 mM, 1.5 eq.) in a scintillation vial and dissolving them in a 1,4-dioxane:mesitylene solution (4:1 v/v, 1 mL). The resulting suspension was sonicated at room temperature until the monomers were completely dissolved. The reactor containing a PAN membrane (see Figure S1) was charged with an aqueous solution of $Sc(OTf)_3$ (5 mM, 0.6 mL), and the organic solution (0.4 mL) was slowly layered on top of the aqueous layer. A glass cylinder (ID 25 mm) was placed on top of the silicone O-ring and covered with a glass plate for 30 min. After this time, the grown film grown was transferred to the PAN by drawing both aqueous and organic solutions through the outlet port of the membrane holder using a needle and syringe. The COF-PAN membrane was gently rinsed with MeOH and subsequently used for performance characterization.

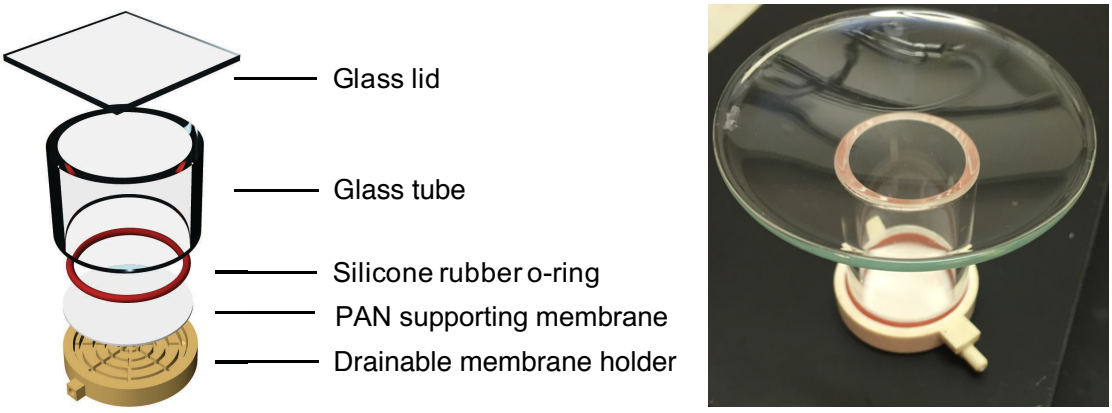

Figure S1. Schematic image and photo of reactor.[6]

C. ^{1}H and ^{13}C NMR Spectra of COF Monomers

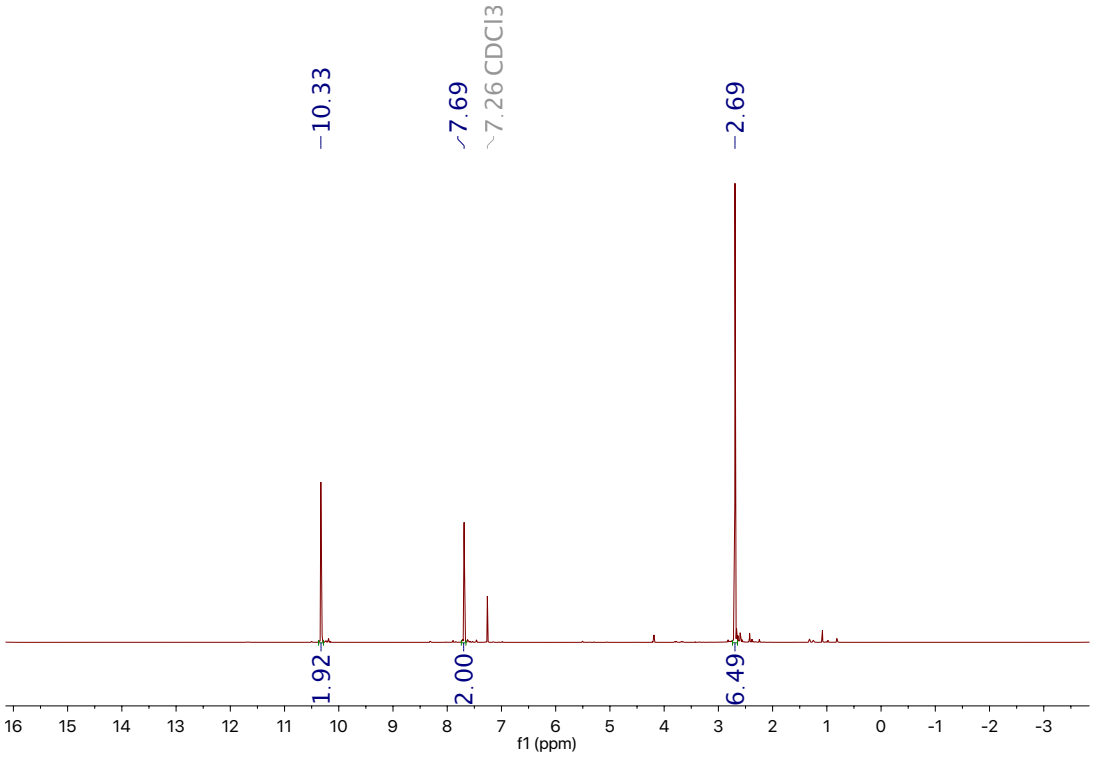

Figure S2. ^{1}H NMR spectrum of **PDA-Me** in $CDCl_3$.

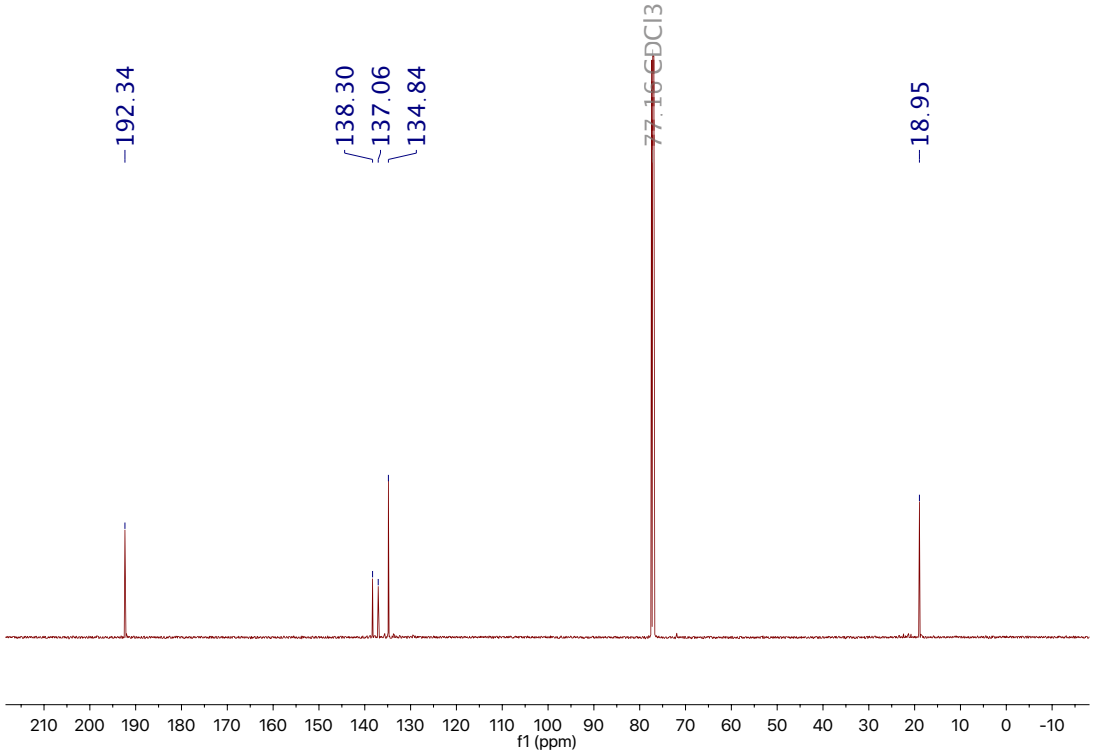

Figure S3. ^{13}C NMR spectrum of **PDA-Me** in $CDCl_3$.

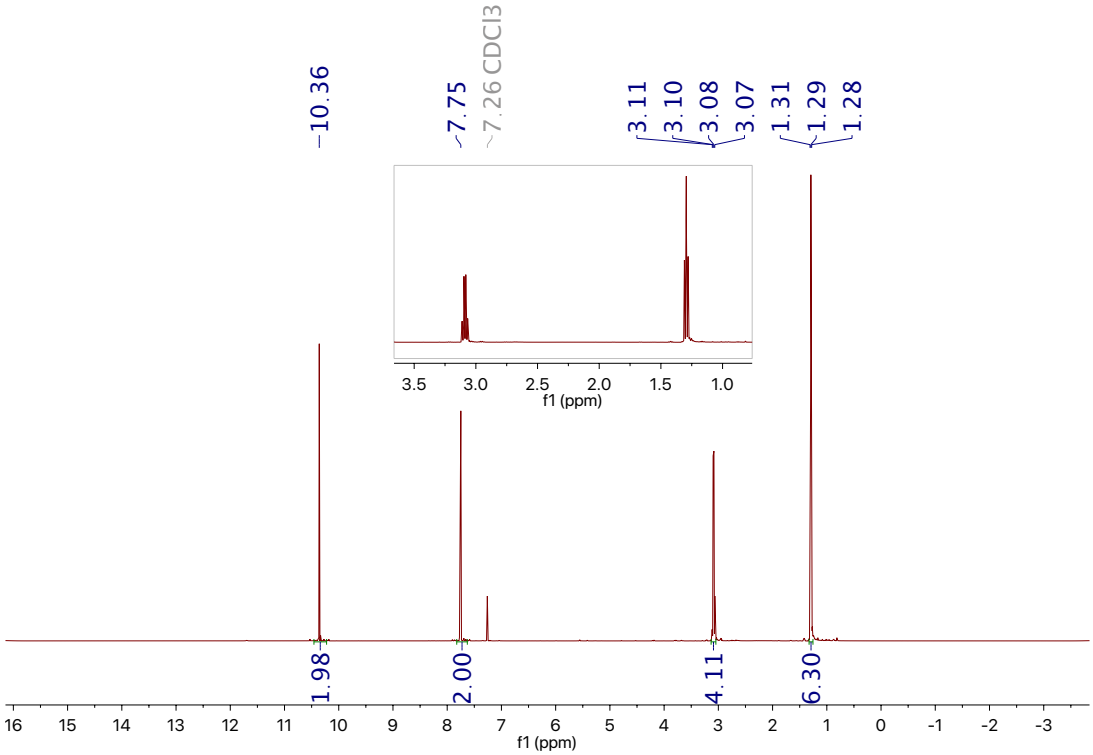

Figure S4. ^{1}H NMR spectrum of **PDA-Et** in $CDCl_3$.

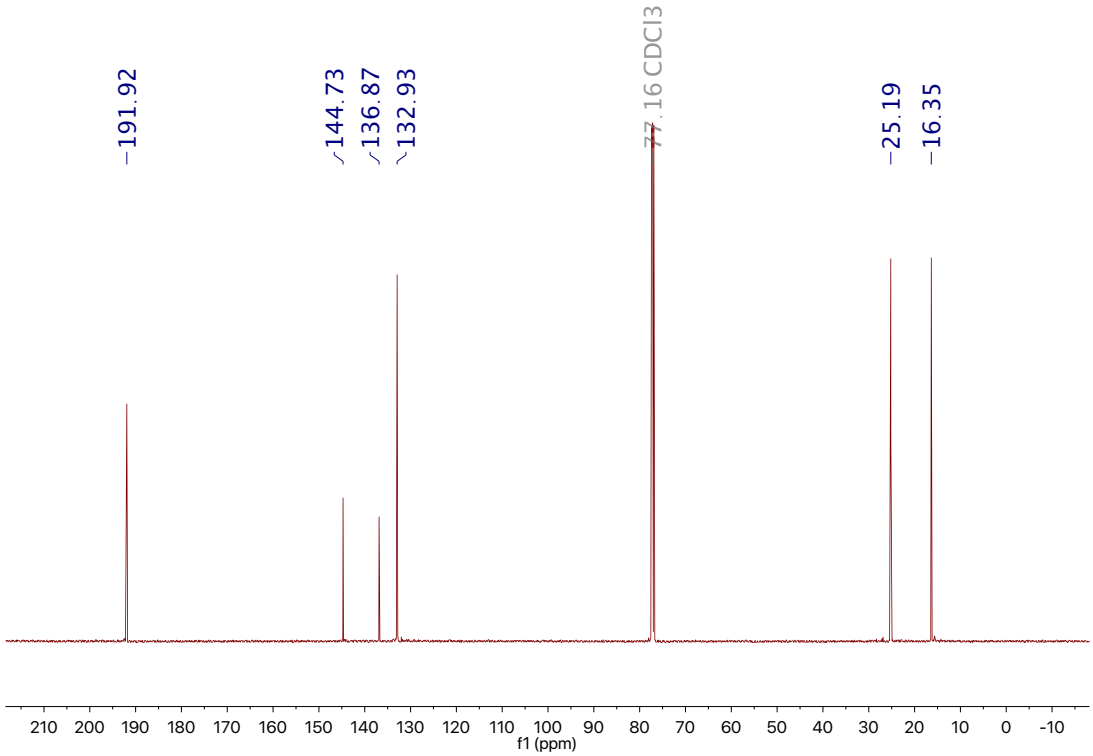

Figure S5. ^{13}C NMR spectrum of **PDA-Et** in $CDCl_3$.

D. Powder X-ray Diffraction Patterns for COF Powders

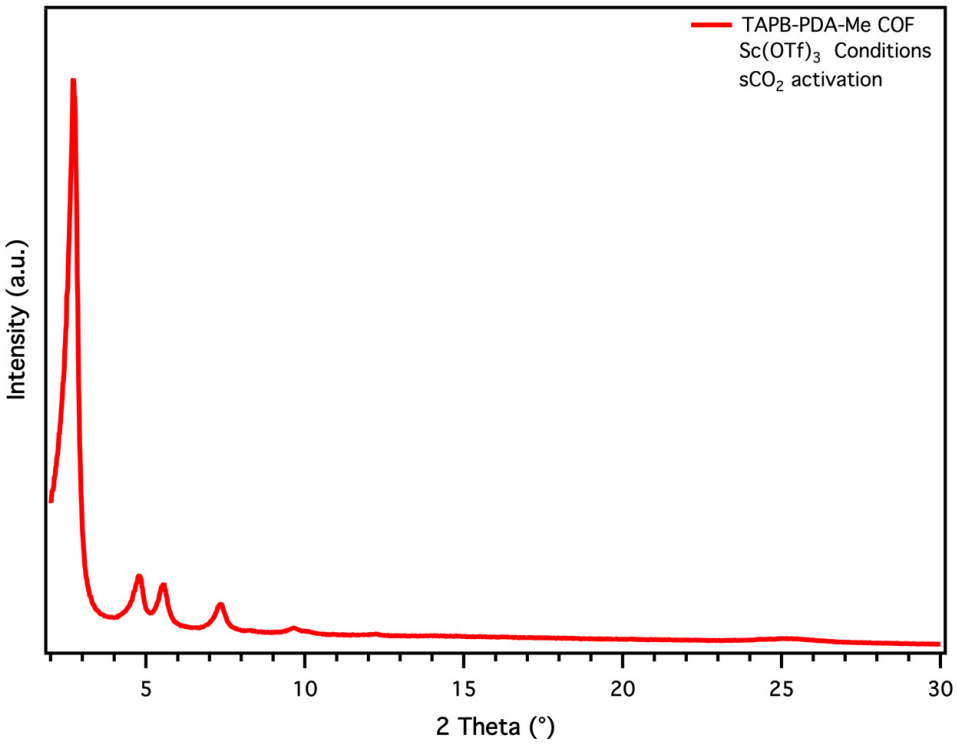

Figure S6. PXRD patterns for **TAPB-PDA-Me** COF powder formed under $Sc(OTf)_3$ conditions.

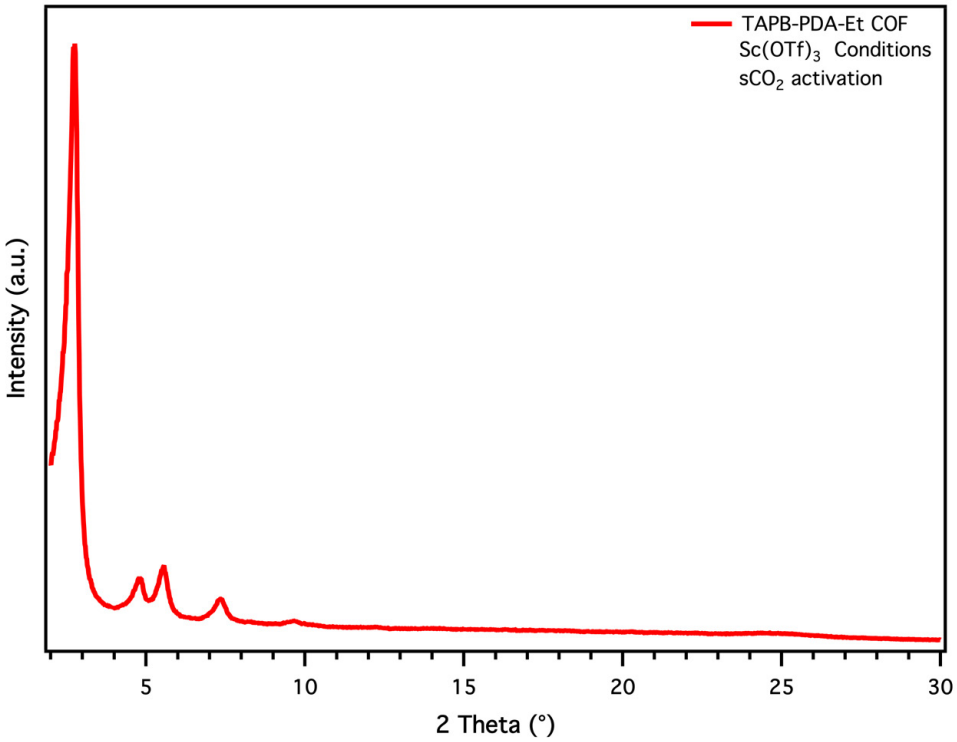

Figure S7. PXRD patterns for **TAPB-PDA-Et** COF powder formed under $Sc(OTf)_3$ conditions.

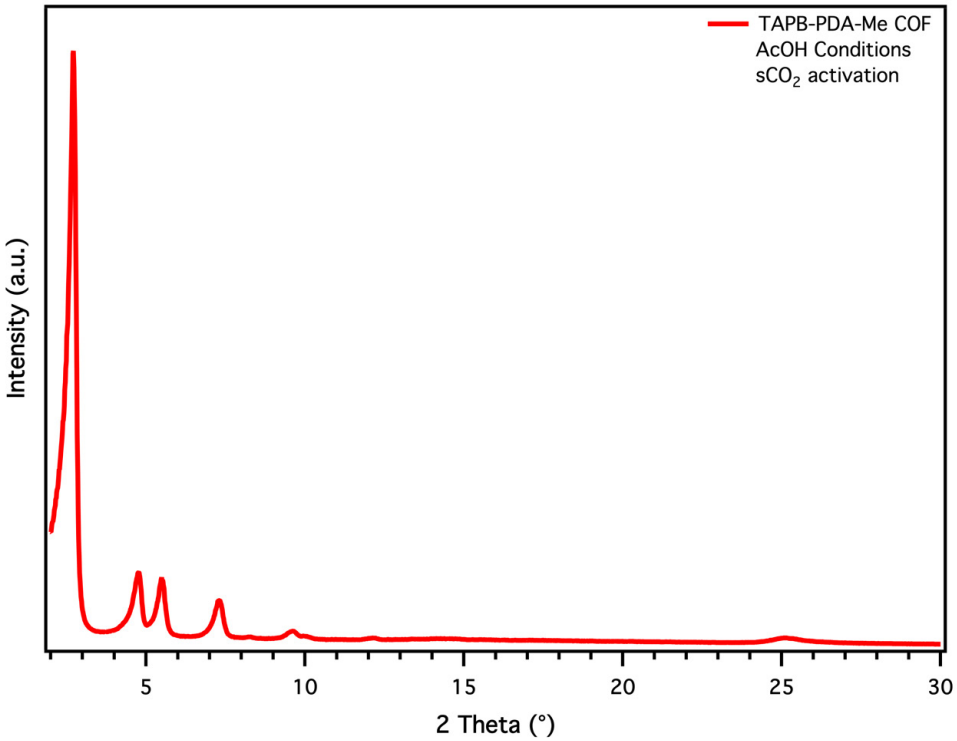

Figure S8. PXRD patterns for **TAPB-PDA-Me** COF powder formed under AcOH conditions.

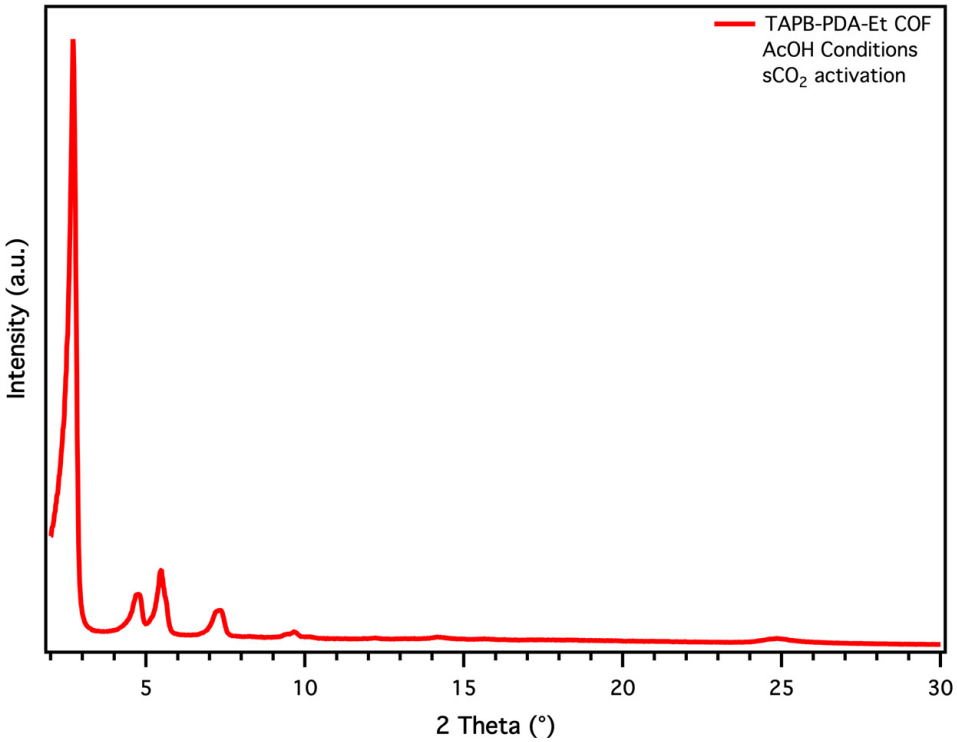

Figure S9. PXRD patterns for **TAPB-PDA-Et** COF powder formed under AcOH conditions.

E. Nitrogen Adsorption Isotherms and BET Plots for Covalent Organic Framework Powders

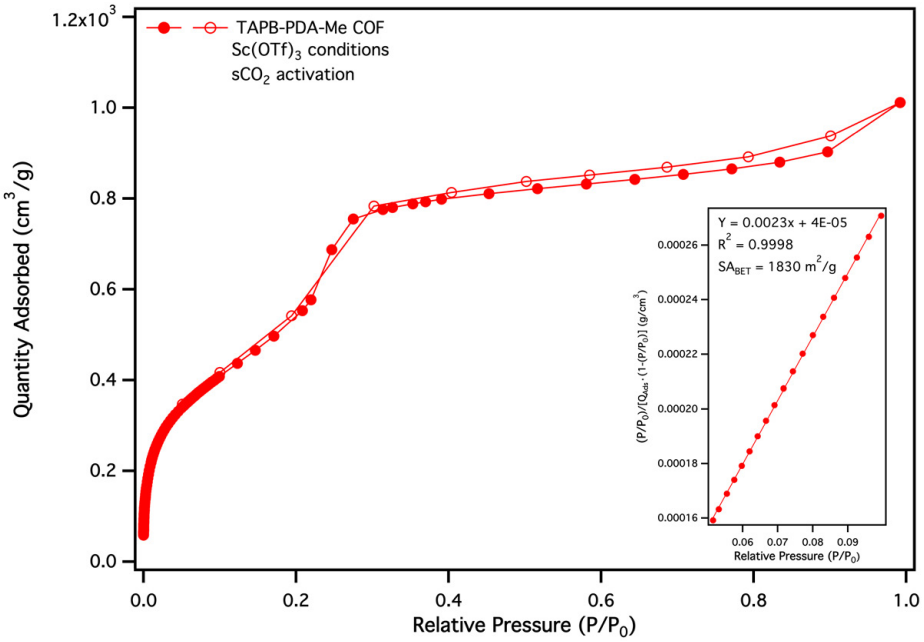

Figure S10. Nitrogen adsorption isotherm for **TAPB-PDA-Me** COF powder prepared under $Sc(OTf)_3$ conditions with the BET plot as an inset.

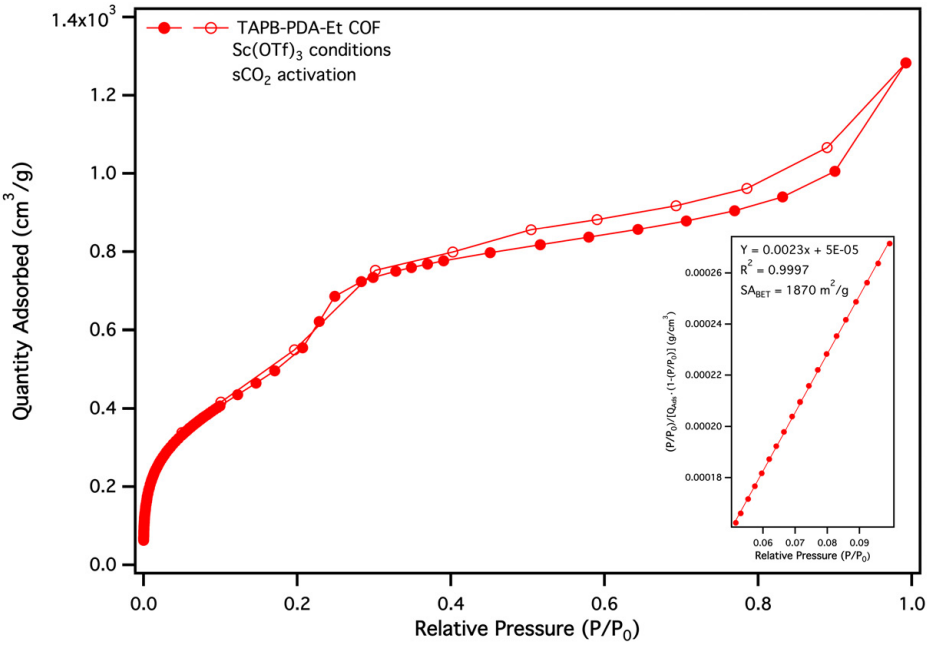

Figure S11. Nitrogen adsorption isotherm for **TAPB-PDA-Et** COF powder prepared under $Sc(OTf)_3$ conditions with the BET plot as an inset.

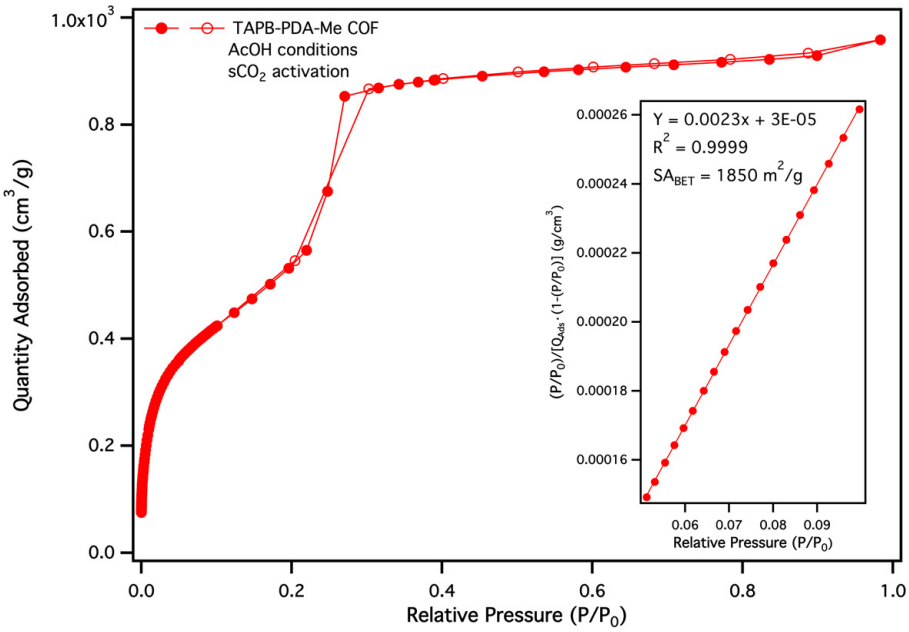

Figure S12. Nitrogen adsorption isotherm for **TAPB-PDA-Me** COF powder prepared under AcOH conditions with the BET plot as an inset.

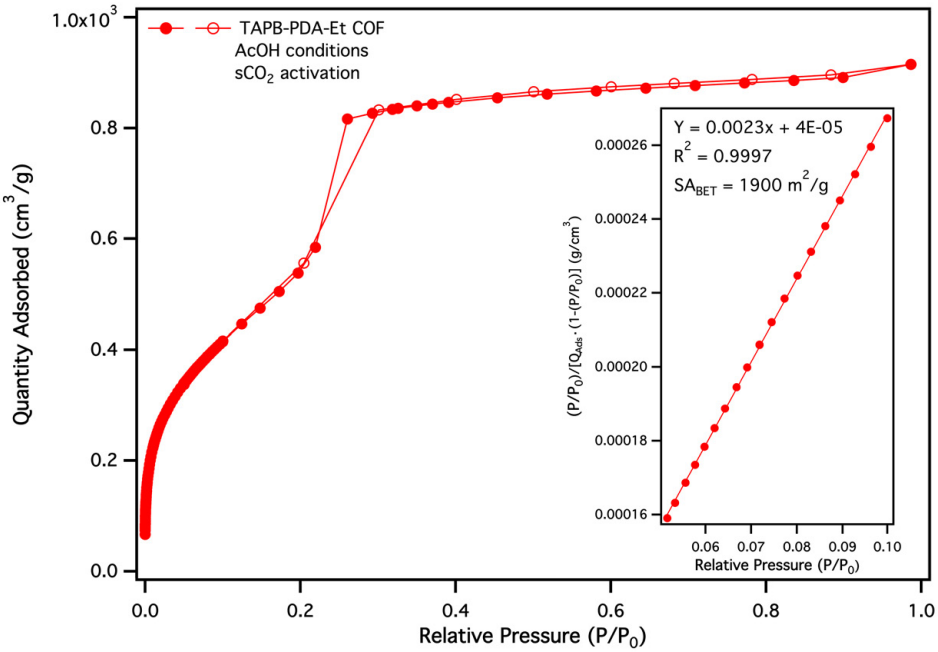

Figure S13. Nitrogen adsorption isotherm for **TAPB-PDA-Et** COF powder prepared under AcOH conditions with the BET plot as an inset.

F. Pore Size Distributions of Covalent Organic Framework Powders

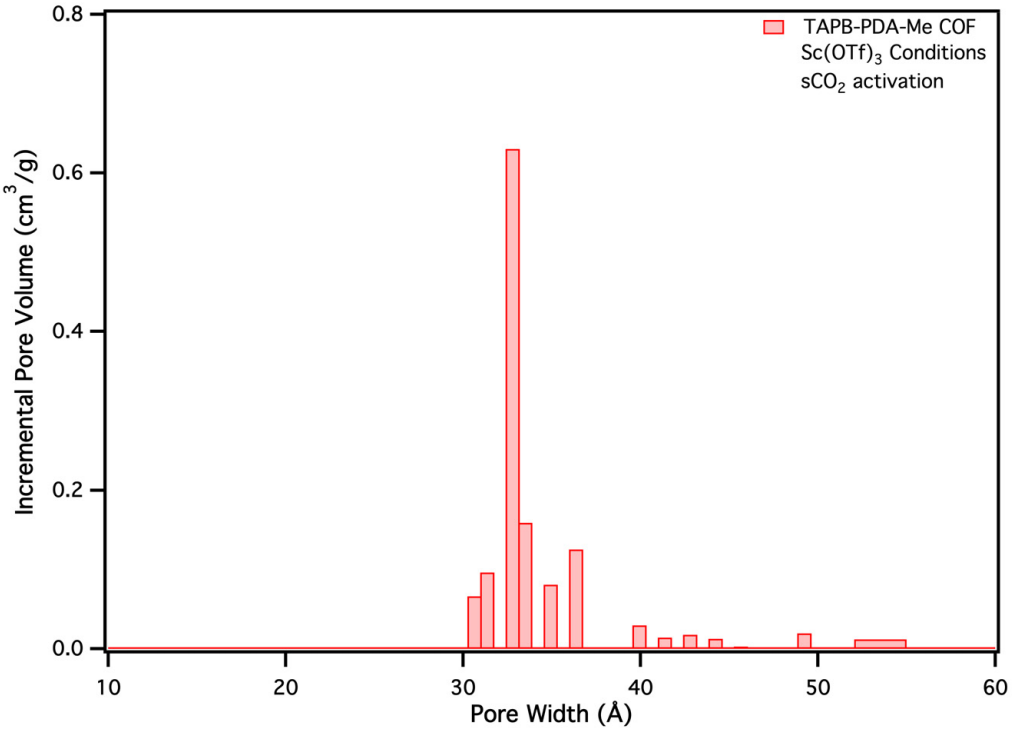

Figure S14. Pore size distribution of **TAPB-PDA-Me** COF powder prepared under $Sc(OTf)_3$ conditions.

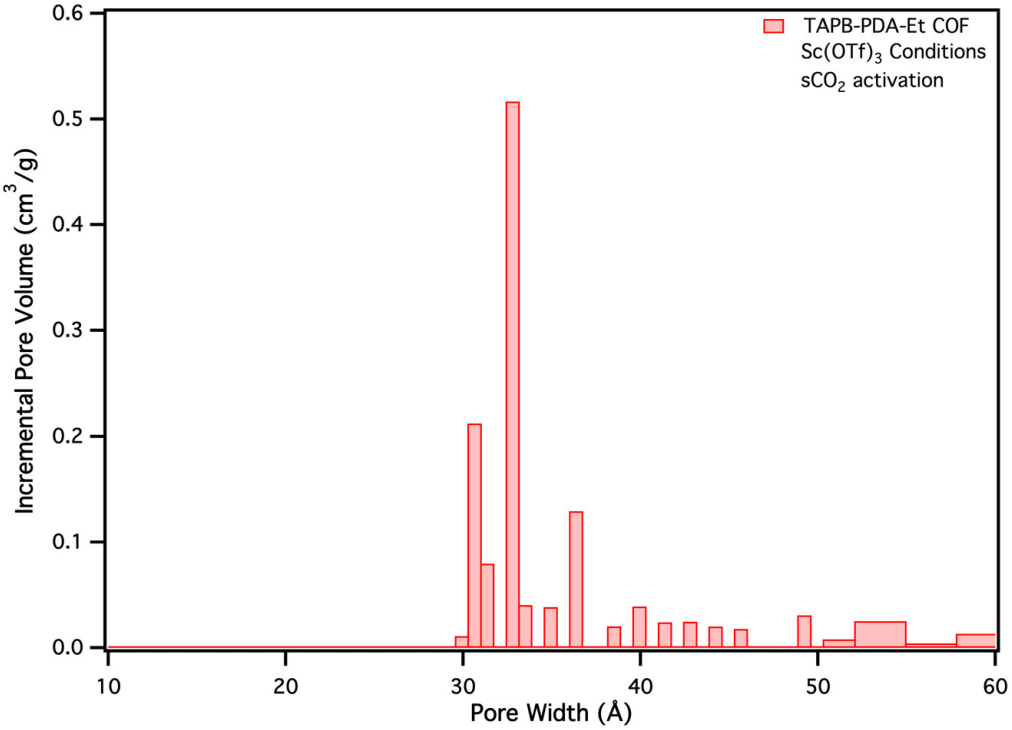

Figure S15. Pore size distribution of **TAPB-PDA-Et** COF powder prepared under $Sc(OTf)_3$ conditions.

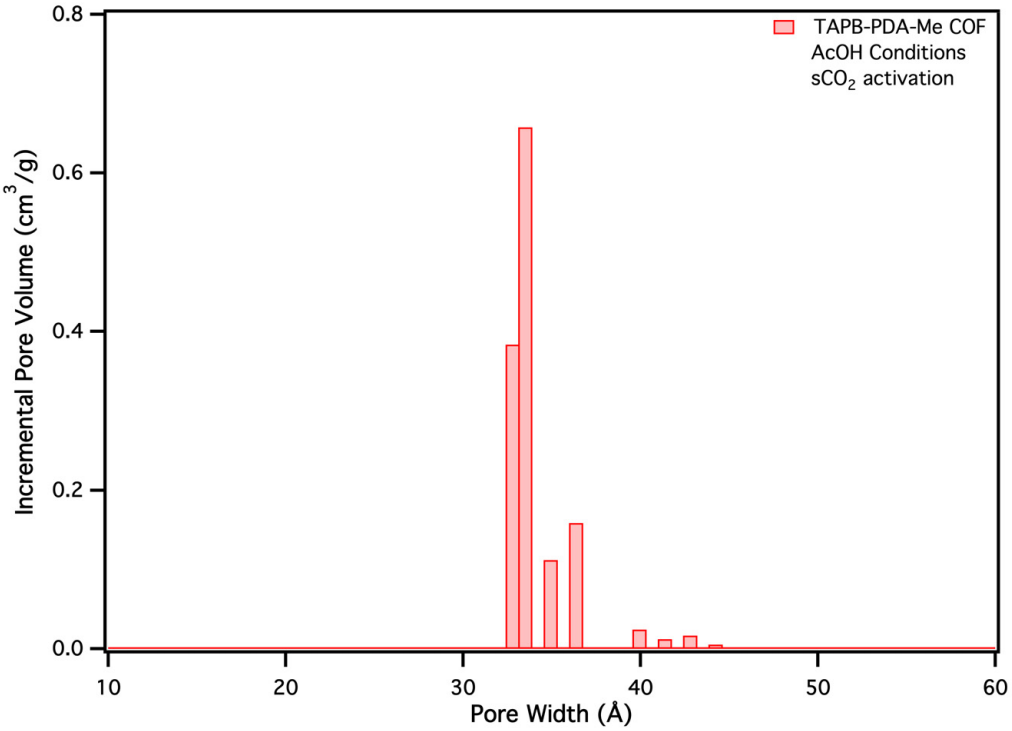

Figure S16. Pore size distribution of **TAPB-PDA-Me** COF powder prepared under AcOH conditions.

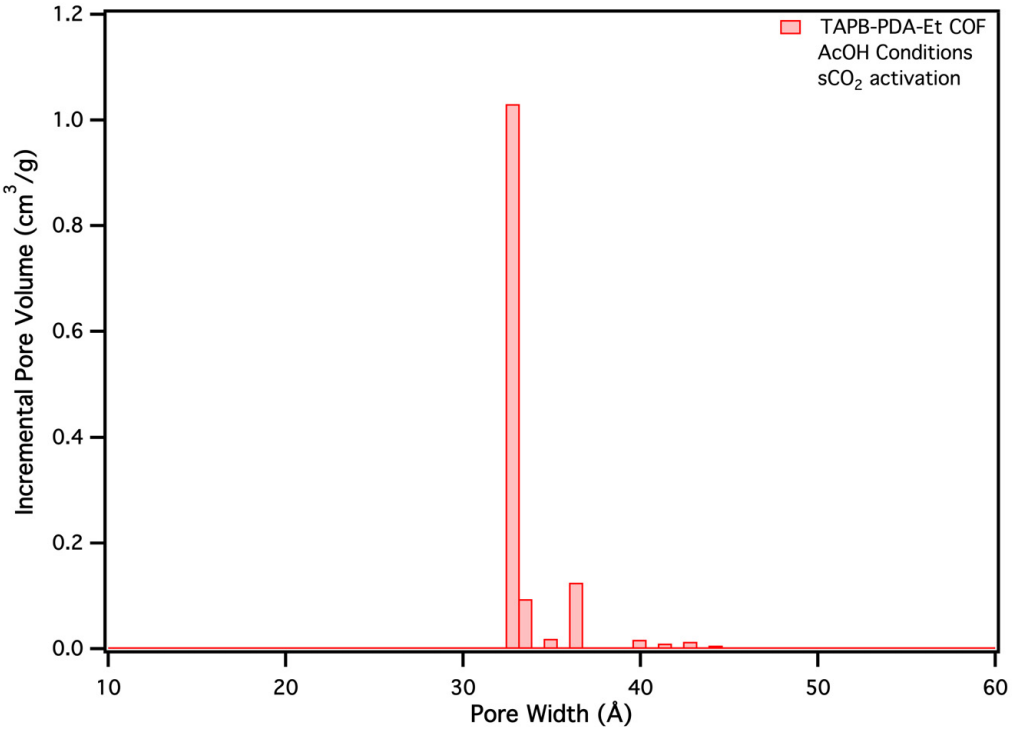

Figure S17. Pore size distribution of **TAPB-PDA-Et** COF powder prepared under AcOH conditions.

G. Vibrational Data

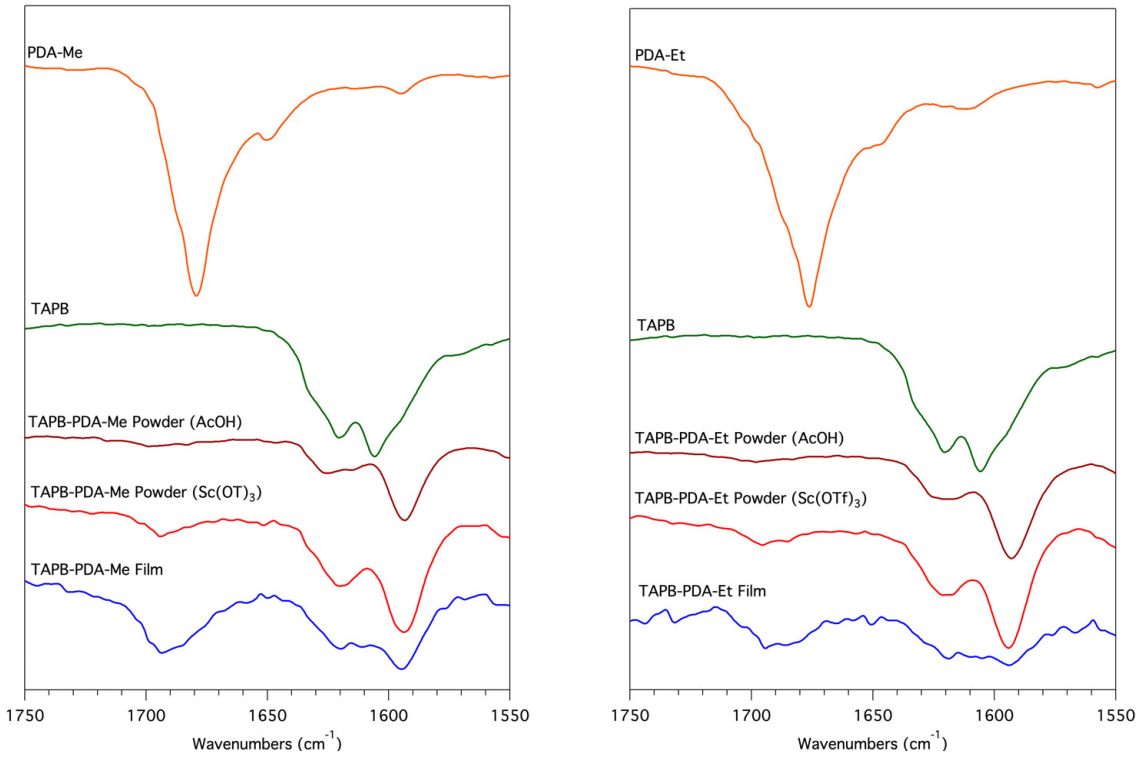

Figure S18. (**Left**) Vibrational data for **TAPB**, **PDA-Me**, and **TAPB-PDA-Me** powders and film. (**Right**) Right Vibrational data for **TAPB**, **PDA-Et**, and **TAPB-PDA-Et** powders and film.

H. Optical Microscopy of COF Films

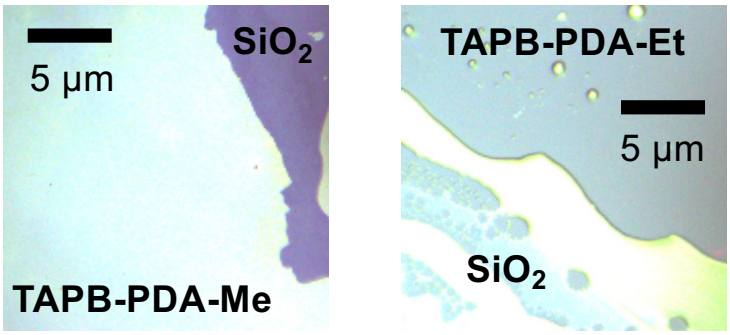

Figure S19. Optical microscopy images of **TAPB-PDA-Me** and **TAPB-PDA-Et** films.

I. Grazing Incidence Wide Angle X-ray Scattering (GI-WAXS) of COF Films

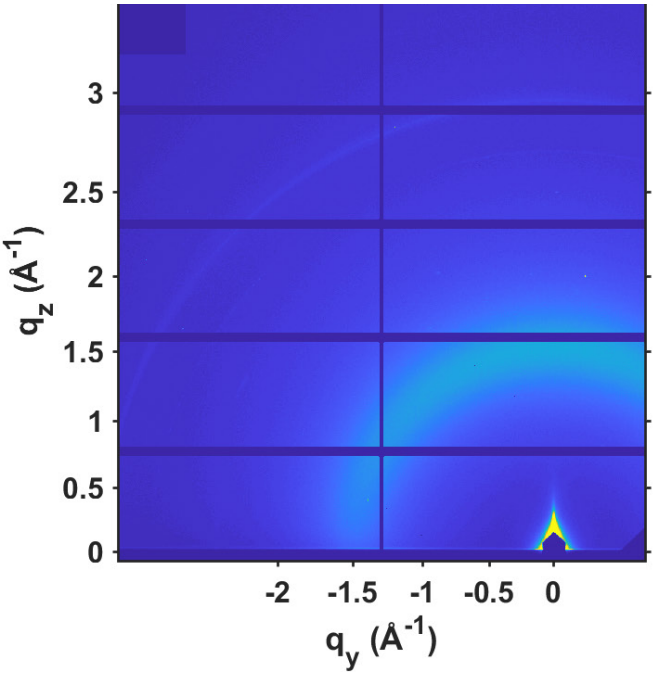

Figure S20. Grazing incidence wide angle X-ray scattering (GI-WAXS) of **TAPB-PDA-H** film on fused silica substrate.

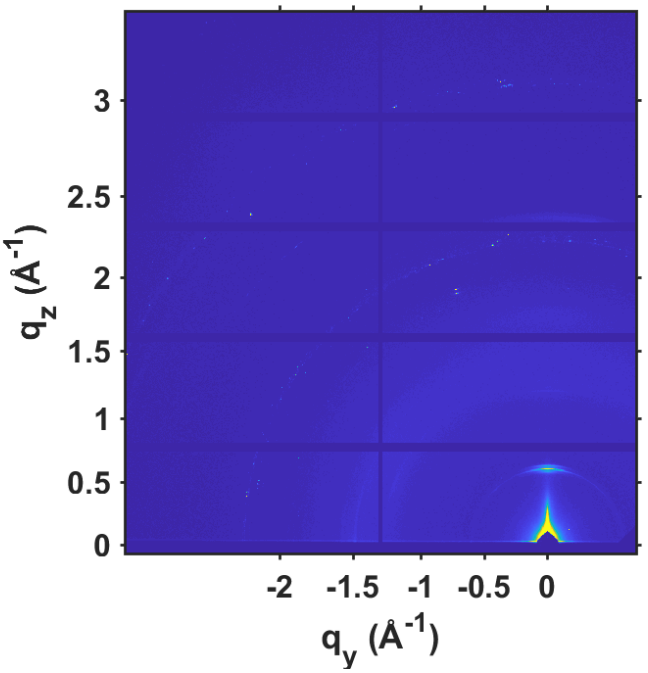

Figure S21. Grazing incidence wide angle X-ray scattering (GI-WAXS) of **TAPB-PDA-Me** film on SiO_2 substrate.

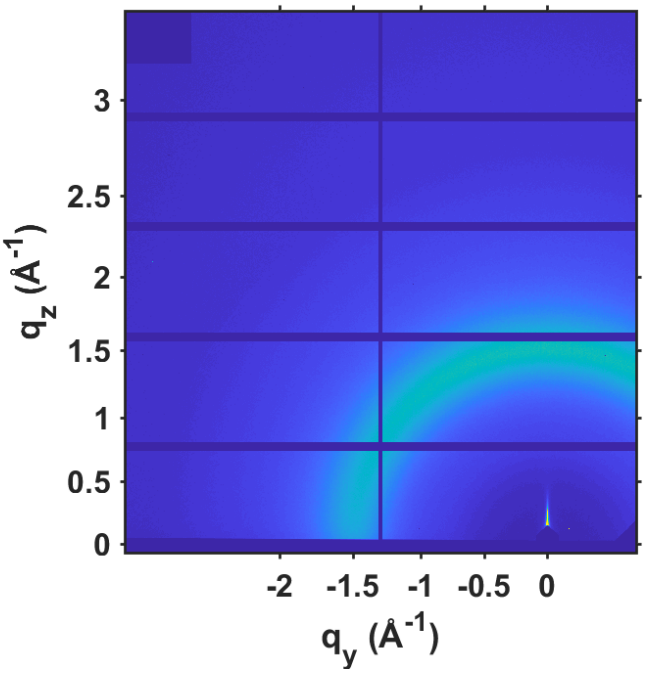

Figure S22. Grazing incidence wide angle X-ray scattering (GI-WAXS) of **TAPB-PDA-Et** film on fused silica substrate.

J. Scanning Electron Microscopy (SEM) Images of Thin-Film Composite COF PAN Membranes

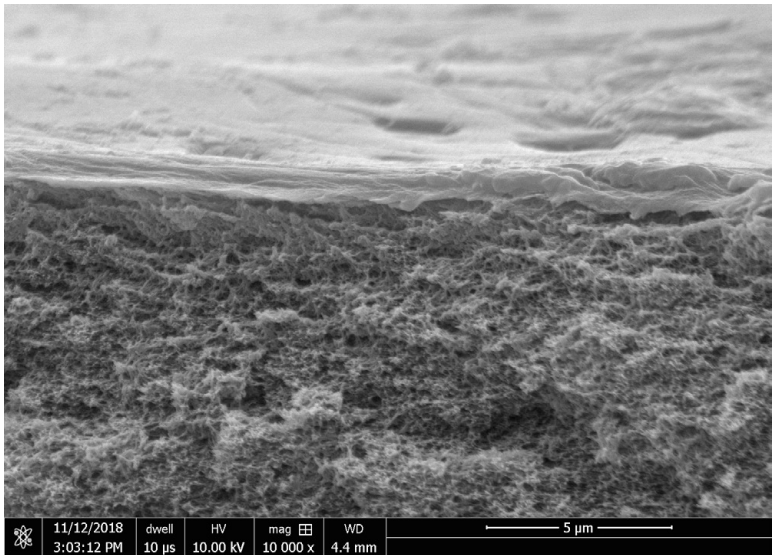

Figure S23. Cross-sectional SEM image of thin-film composite PAN membrane containing **TAPB-PDA-H** active layers.

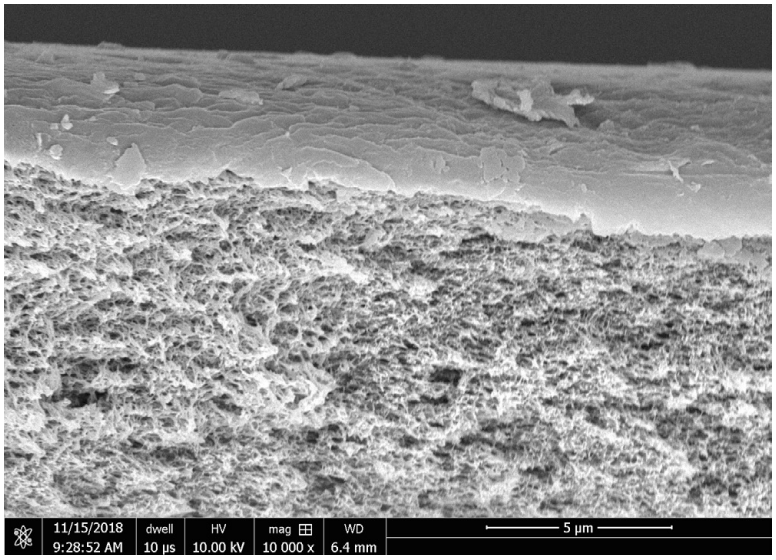

Figure S24. Cross-sectional SEM image of thin-film composite PAN membrane containing **TAPB-PDA-Et** active layers.

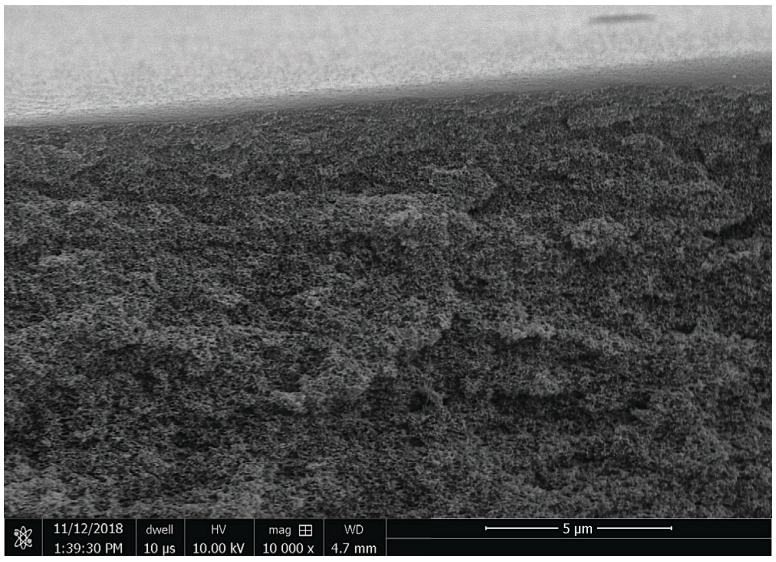

Figure S25. Cross-sectional SEM image of pristine PAN.

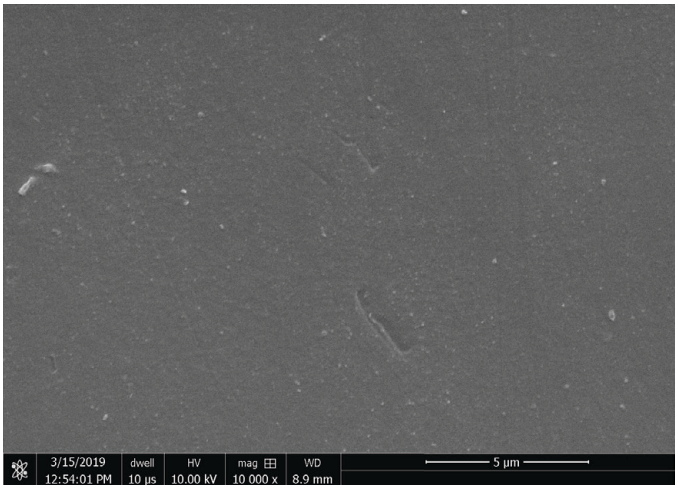

Figure S26. Top view SEM image of **TAPB-PDA-H** on PAN.

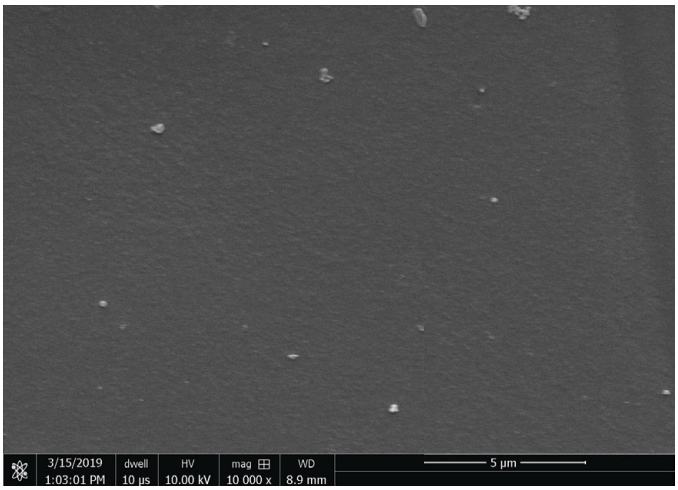

Figure S27. Top view of SEM image of **TAPB-PDA-Me** on PAN.

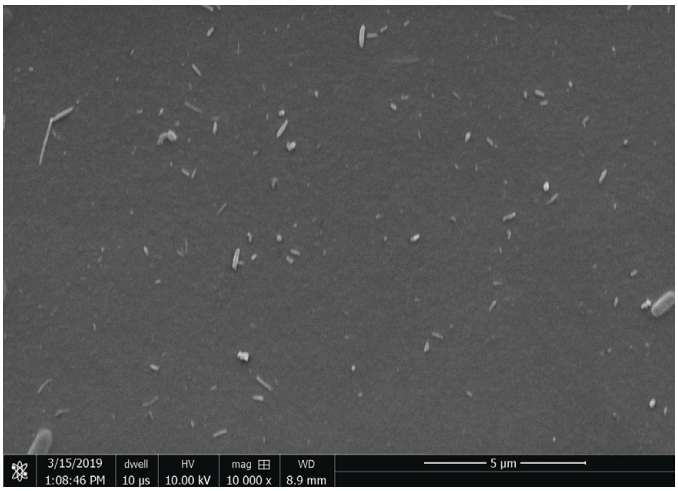

Figure S28. Top view of SEM image of **TAPB-PDA-Et** on PAN.

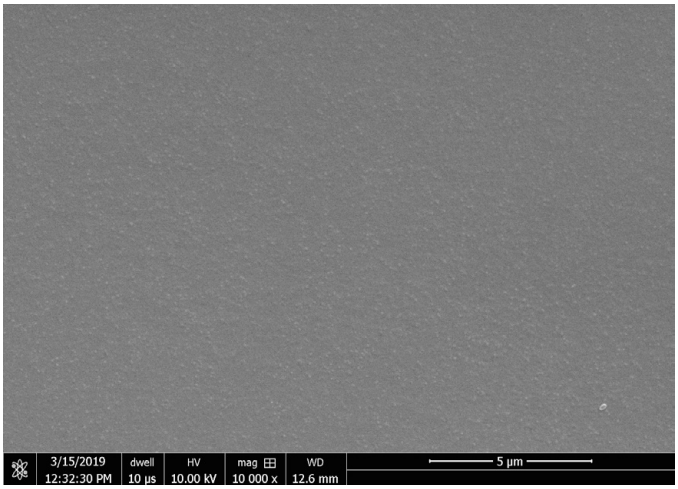

Figure S29. Top view of SEM image of pristine PAN.

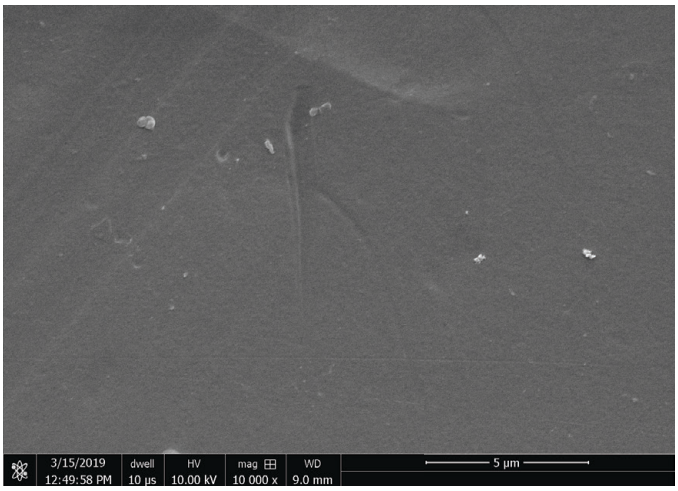

Figure S30. Top view of SEM image of control PAN.

K. Solution-Diffusion Model Equations

$$\textbf{Eq. 1}: \quad Rejection\ (\%) = 1 - \frac{C_p}{C_f} = \frac{100}{1+\left[\frac{B}{(1-\alpha)J_v}+\frac{\alpha}{1-\alpha}\right]\exp\left(\frac{J_v}{k}\right)}$$

$$\textbf{Eq. 2}: Rejection\ (\%) = 1 - \frac{C_p}{C_f} = \left[100 - \frac{100}{1+\frac{(J_v - B_{COF} - \alpha_{COF}J_V)+B_{COF}(J_V+B_{SUPPORT})/(B_{SUPPORT}+\alpha_{SUPPORT}J_V)}{(B_{COF}+\alpha_{COF}J_V)*\exp\left(\frac{J_V}{k}\right)}}\right]$$

L. Permeate Water Flux as a Function of Hydraulic Pressure

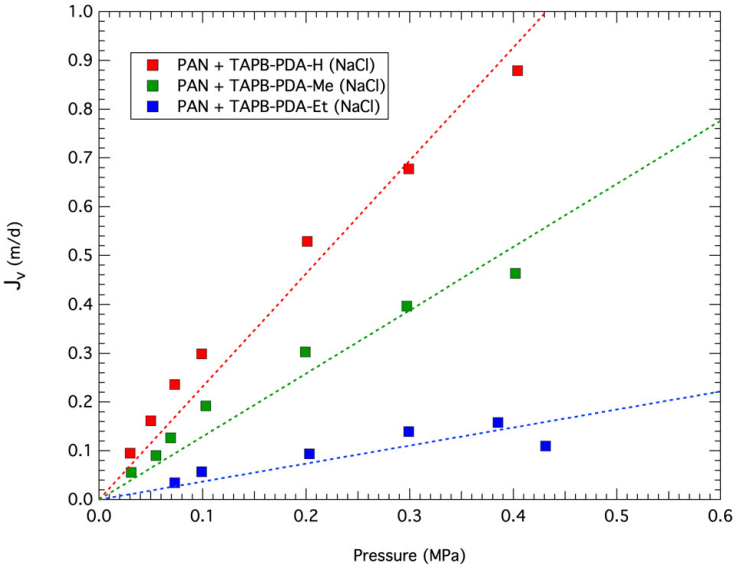

Figure S31. Permeate water flux J_v as a function of hydraulic pressure obtained for thin-film composite polyacrylonitrile (PAN) membranes with COF active layers of **TAPB-PDA-H**, **TAPB-PDA-Me**, or **TAPB-PDA-Et** tested with NaCl solutions.

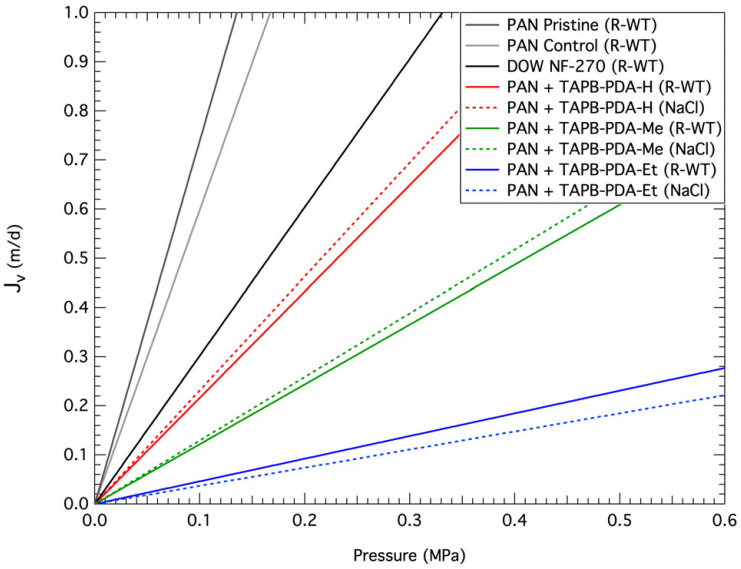

Figure S32. Direct comparison of regression lines from Figures 4 and S31. Permeate water flux J_v as a function of hydraulic pressure obtained for thin-film composite polyacrylonitrile (PAN) membranes with COF active layers of **TAPB-PDA-H**, **TAPB-PDA-Me**, or **TAPB-PDA-Et** tested with R-WT or NaCl solutions. Regression lines are also shown for corresponding pristine and control PAN supports without the COF layer, and for commercial nanofiltration (NF) membrane (DOW FILMTEC NF-270) tested with R-WT solutions.

M. References

1. Wessig, P.; Gerngroß, M.; Freyse, D.; Bruhns, P.; Przezdziak, M.; Schilde, U.; Kelling, A., Molecular Rods Based on Oligo-spiro-thioketals. *J. Org. Chem.* **2016,** *81* (3), 1125-1136.
2. Cook, M.; Gaffney, P. R. J.; Peeva, L. G.; Livingston, A. G., Roll-to-roll dip coating of three different PIMs for Organic Solvent Nanofiltration. *J. Membrane Sci.* **2018,** *558*, 52-63.
3. Matsumoto, M.; Dasari, R. R.; Ji, W.; Feriante, C. H.; Parker, T. C.; Marder, S. R.; Dichtel, W. R., Rapid, Low Temperature Formation of Imine-Linked Covalent Organic Frameworks Catalyzed by Metal Triflates. *J. Am. Chem. Soc.* **2017,** *139* (14), 4999-5002.
4. Smith, B. J.; Overholts, A. C.; Hwang, N.; Dichtel, W. R., Insight into the crystallization of amorphous imine-linked polymer networks to 2D covalent organic frameworks. *Chem. Commun.* **2016,** *52* (18), 3690-3693.
5. Valentino, L.; Matsumoto, M.; Dichtel, W. R.; Mariñas, B. J., Development and Performance Characterization of a Polyimine Covalent Organic Framework Thin-Film Composite Nanofiltration Membrane. *Environ. Sci. Technol.* **2017,** *51* (24), 14352-14359.
6. Matsumoto, M.; Valentino, L.; Stiehl, G. M.; Balch, H. B.; Corcos, A. R.; Wang, F.; Ralph, D. C.; Mariñas, B. J.; Dichtel, W. R., Lewis-Acid-Catalyzed Interfacial Polymerization of Covalent Organic Framework Films. *Chem* **2018,** *4* (2), 308-317.